Decoupling the effects of defects on efficiency and stability through phosphonates in stable halide perovskite solar cells

Haibing Xie,[1†] Zaiwei Wang,[2†] Zehua Chen,[3] Carlos Pereyra,[1] Mike Pols,[3] Krzysztof Gałkowski,[4] Miguel Anaya,[4] Shuai Fu,[5] Xiaoyu Jia,[5] Pengyi Tang,[1] Dominik Józef Kubicki,[6,7] Anand Agarwalla,[2] Hui-Seon Kim,[2] Daniel Prochowicz,[6,8] Xavier Borrisé,[9] Micha Bonn,[5] Chunxiong Bao,[10] Xiaoxiao Sun,[11] Shaik Mohammed Zakeeruddin,[6] Lyndon Emsley,[7] Jordi Arbiol,[1,12] Feng Gao,[10] , Fan Fu,[11] Hai I. Wang,[5] Klaas-Jan Tielrooij,[1] Samuel D. Stranks,[4] Shuxia Tao,[3] Michael Grätzel,[6] Anders Hagfeldt,[2*] Monica Lira-Cantu[1,2*]

1. Catalan Institute of Nanoscience and Nanotechnology (ICN2), CSIC and the Barcelona Institute of Science and Technology (BIST). Building ICN2, Campus UAB E-08193, Bellaterra, Barcelona, Spain.

2. Laboratory of Photomolecular Science (LSPM), Institute of Chemical Sciences and Engineering, School of Basic Sciences, Ecole Polytechnique Fédérale de Lausanne, CH-1015 Lausanne, Switzerland.

3. Center for Computational Energy Research, Applied Physics, Eindhoven University of Technology, Eindhoven, the Netherlands.

4. Cavendish Laboratory, University of Cambridge, Cambridge, UK.

5. Max-Planck Institute for polymer Research, Ackermannweg 10, Mainz, Germany.

6. Laboratory for Photonics and Interfaces (LPI), Institute of Chemical Sciences and Engineering, School of Basic Sciences, Ecole Polytechnique Fédérale de Lausanne, CH-1015 Lausanne, Switzerland.

7. Laboratory of Magnetic Resonance (LRM), Institute of Chemical Sciences and Engineering, School of Basic Sciences, Ecole Polytechnique Fédérale de Lausanne, CH-1015 Lausanne, Switzerland.

8. Institute of Physical Chemistry, Polish Academy of Sciences, Kasprzaka 44/52, 01-224 Warsaw, Poland.

9. Institute of Microelectronics of Barcelona IMB-CNM, C/del Til·lers., Cjampus Universitat Autònoma de Barcelona (UAB) 08193, Cerdanyola del Vallès (Bellaterra), Barcelona, Spain.

10. Department of Physics, Chemistry and Biology (IFM), Linköping University, Linköping, Sweden.

11. Laboratory for Thin Films and Photovoltaics, Empa—Swiss Federal Laboratories for Materials Science and Technology, Ueberlandstrasse 129, Duebendorf, 8600, Switzerland

12. ICREA, Pg. Lluís Companys 23, 08010 Barcelona, Catalonia, Spain.

† These authors contributed equally to this work.

* Corresponding authors: anders.hagfeldt@epfl.ch; monica.lira@icn2.cat

SUMMARY

The understanding of defects is of paramount importance for the development of stable halide perovskite solar cells (PSCs). However, isolating their distinctive effects on the device efficiency and stability is currently a challenge. Here, we report that adding the organic molecule 3-phosphonopropionic acid (H3pp) to the halide perovskite precursor solution results in unchanged overall optoelectronic performance while having a tremendous impact on the stability of the halide perovskite by means of ion immobilization. As a result, we obtained PSCs with ~21 % efficiency and outstanding operational stability, retaining nearly 100 % of the initial efficiency after 1000 h at the maximum power point under simulated AM1.5 illumination. The strong interaction between the perovskite and the H3pp molecule through two types of hydrogen bonds (H$\cdots$I and O$\cdots$H) from the phosphonate group allows immobilization of ions that leads to remarkable device stability. This binding mode results in shallow point defect passivation that has a significant impact on the device stability but not on the nonradiative recombination and device efficiency. We expect that decoupling the effect of defects on the efficiency and stability will have important implications for the current understanding and advancement of operational PSCs.

Keywords

Perovskite solar cells, performance, stability, additive engineering, defect passivations, shallow point defects, deep point defects, phosphonates

INTRODUCTION

Photovoltaic (PV) energy technologies are crucial to transform our society into a low-carbon economy, enabling the production of electricity from sunlight. Single-junction halide perovskite solar cells (PSCs) have already achieved a certified power conversion efficiency (PCE) above 25 %.[1,2] Despite their excellent PV performance, operational stability remains the main obstacle for the deployment of this technology. The PCE and operational stability in PSCs are thought to be strongly interrelated through the defect density at the surface, grain boundaries, interfaces and in the bulk of the halide perovskite (HP).[2] Defects can either boost charge transport (generating extra free charge carriers by doping) or impede it by trapping or scattering the carriers.[3]

Defects associated with deep trap states in HP (e.g. undercoordinated halides ions, undercoordinated Pb^{2+} ions) promote non-radiative recombination, leading against a high photovoltage, hampering the ultimate device efficiency.[4] Shallow defects, on the contrary, are considered benign in classical inorganic semiconductors and have little contribution to non-radiative recombination, not strongly influencing the efficiency of the device.[5] This high tolerance to shallow defects is what makes the perovskite family known as *defect-tolerant.*[5] However, the ionic-electronic characteristics of HPs, together with their "soft material" nature, indicates a strong ionic component where charged shallow level traps with low formation energies (e.g. I or MA vacancies), results unfavourable for the solar cell, causing ion migration, phase segragation and hysteresis.[5-7] This is especially detrimental for the PSC under non-equilibrium conditions, such as high temperature, electrical bias, continuous light irradiation or their combination, where ion migration dictates the long-term stability of operational PSCs.[8-10] The introduction of additives (organic or inorganic compounds) into the HP layer is a method that has been effectively applied to passivate defects to increase the efficiency of the solar cell.[11-13] The success of such an approach is not straight forward and depends on multiple factors like HP thin film preparation, nature of precursors, type of additives.[14-18] Although efficient PSCs can be fabricated following this strategy and the stability is enhanced if compared with the control device without additive, the real outcome is not always stable PSC as defined as those able to display less than 10 % degradation after 1000 h of continuous illumination under 1 sun.[19] Thus, in order to attain highly efficient and stable PSCs it is not only important to passivate defects responsible for deep level traps that results in high efficiency. It is also important to ensure ion immobilization through the passivation of defect-induced shallow level traps.[6,7]

The ionic motion is defined by the energy barriers to ionic transport in the HP, where halide ions (I^-) and organic cations (MA, FA) are the main mobile ions.[8,15,20,21] The binding mode between an additive and the HP plays a critical role in the migration of ions, and determines the optoelectronic properties of the device and its long-term stability. Additives with functional groups S=O, P=O or C=O can control

the HP crystallization, passivate uncoordinated Pb^{2+} defects or both. Hydroxyl (-OH) and carboxyl (-COOH) groups also act as Lewis bases passivating uncoordinated lead defects by forming Pb-O bonds[22]. In particular, the hydrogen bonding energy between organic cations and PbI_6^{4-} octahedra, as well as Pb-I bonds, weakens under continuous illumination. This effect facilitates the migration of both the organic cations and the halide anions in an HP, which would accelerate its decomposition in the absence of stabilizing additives.[21] The chemical shift trend for an additive varies considerably depending on the functional group participating in the bonding with the HP. In PSCs, the most employed additives ==includes== functional groups such as $-COOH$ or $-NH_3^+$, while $-PO(OH)_2$ is less employed.[16,23,24,18,25] The peculiar behaviour of the phosphonic acid derivative has been related to a stronger H-donating character,[26] which also plays an essential role in charge injection. Bonding through the phosphonic acid group has been reported to be more stable than bonding through carboxylic or amine groups, although the charge injection rates can be affected by the tetrahedral phosphorous centre and loss of conjugation.[27] For example, Brown *et al*. analysed the advantages of both $-PO(OH)_2$ and $-COOH$ anchoring agents in solar cells: $-PO(OH)_2$ was employed to increase the surface binding stability, and carboxylic acids were employed to increase the electron injection efficiency.[28] This indicates that the chemical bonding between the HP and the additive also plays an important role on the regulation of the activation energy of ion migration, which determines the long-term stability of PSCs.[10] However, despite all these research efforts, the understanding of the binding modes in perovskite-additive interactions and the correlation between defect passivation, non-radiative recombination and device efficiency and stability remain poorly understood.

In this work, we study the addition of the 3-phosphonopropionic acid (H3pp) organic molecule to an HP absorber and investigate the effect that two different anchoring groups (phosphonate $-PO(OH)_2$ and carboxylate $-COOH$) have on the performance and stability of PSCs. In order to ensure an accurate comparison between the different characterization methods carried out to materials, thin films and complete devices, all our studies were carried out at room temperature. We fabricate complete solar cells with the configuration $FTO/c-TiO_2/m-TiO_2/HP/Spiro-OMeTAD/Au$ based on the multication perovskite absorber with the nominal formula $Rb_{0.05}Cs_{0.05}MA_{0.15}FA_{0.75}Pb_{1.05}(I_{0.95}Br_{0.05})_3$ (RbCsMAFA)[29] with and without the H3pp molecule. The PSCs showed excellent and similar overall optoelectronic performance and remarkable device stability, leading to PSCs with an open-circuit voltage of V_{oc} ~1.1 V and a PCE of ~21 %. Surprisingly, stability analyses of the PSC with H3pp showed negligible loss of the initial efficiency after 1000 h under 1 sun and maximum power point (MPP) tracking, while the reference device (without H3pp) showed > 20 % loss under the same conditions. To understand the effect of the H3pp molecule on the optoelectronic properties of the perovskite and its stability, we employed contactless high-throughput characterization, including time-resolved photoluminescence

(TRPL) spectroscopy, photoluminescence quantum efficiency (PLQE) measurement, optical-pump THz-probe (OPTP) spectroscopy and thermal admittance spectroscopy (TAS). First-principles density functional theory (DFT) calculations, supported by Fourier-transform infrared spectroscopy (FTIR) analyses, demonstrate the presence of two types of hydrogen bonds (H··I and O··H) between the – PO(OH)$_2$ functional group and the perovskite. These strong binding modes occur through shallow point defects (e.g., FA and I vacancies)[30,31] that block or immobilize ions, resulting in remarkable device stability. This interaction is also benign to the electronic structure of the perovskite and is not related to nonradiative recombination, as opposed to other binding modes that influence electronic interactions and passivate by binding directly to vacancy/defect sites.[32-34] We expect our findings to enable decoupling of the effects of defects on the efficiency and stability to advance on the understanding of shallow and deep defect passivation, non-radiative recombination and PSC performance.

RESULTS AND DISCUSSION

Photovoltaic performance

Different organic additives sharing the phosphonic, –PO(OH)$_2$, and carboxylic acid, –COOH, functional groups with different structures and chain lengths (**Figure S1**) were initially selected. These two functional groups were chosen due to the known interaction with the HP and the transport layers.[27,28,35-38] In all cases, the PCEs were below those obtained for the reference RbCsMAFA device (**Figure S1**). The best PV efficiency was observed for H3pp, one of the smallest and simplest molecules in the catalogue we explored. After careful optimization of its concentration within the HP, the 1:500 H3pp:HP ratio resulted in PSCs with the highest PCE, comparable to that of the reference PSCs (**Figure S2**). A scanning electron microscopy (SEM) cross-sectional image of the HP:H3pp PSC is depicted in **Figure 1a**. The champion PSC fabricated with H3pp shows PCEs of 21.22 % and 20.45 % in reverse and forward scans, respectively (**Figure 1b and Figure S3**), with a stabilized PCE of 21.1 % (inset of **Figure S3**). The J$_{sc}$ from the IV curves agrees with the integrated J$_{sc}$ obtained from the incident photon-to-electron conversion efficiency (IPCE) analysis (**Figure S4**). The optimization of the fabrication process statistically yielded average PCEs of 20.2 ± 0.7 % and 20.6 ± 0.4 % and an average V$_{oc}$ of 1.12 ±0.01 V for the reference and H3pp:HP PSCs, respectively (**Figure 1c and Figure 1d**). Both types of PSCs also demonstrate similar values in their other PV parameters (current density (J$_{sc}$), fill factor (FF) and hysteresis index (HI)) (**Figure S5**).

To evaluate the recombination in our PSCs, we carried out light intensity-dependent V$_{oc}$ analysis in complete devices. Analyses were carried out in devices with the configuration FTO/c-TiO$_2$/m-TiO$_2$/HP/Spiro-OMeTAD/Au, with and without the H3pp additive in the HP layer (**Figure S6a**). The

diode ideality factor (n_{id}) can be extracted from the relation $V_{oc} = E_g + (n_{id}kT/q) \ln(I/I_0)$, where E_g is the band gap, k is the Boltzmann constant, T is the temperature, q is the elementary charge, and I_0 is a reference intensity usually at one sun.[39] Ideality factors with n_{id} =1.80 and 1.85 for PSCs with and without the H3pp were observed, suggesting very similar p-n junction quality and trap-assisted recombination in both types of PSCs,[40,41] in agreement with the similar V_{oc} and efficiency observed. Transient photocurrent (TPC) and open-circuit voltage decay (OCVD) analyses also displayed similar carrier transport and recombination properties for the PSCs with and without the H3pp additive, consistent with the similar J_{sc} and V_{oc} values obtained (**Figure S6b-c**).

Figure 1. PV performance. a, *SEM cross-sectional image of the PSCs with the H3pp:HP material as the absorber.* **b,** *Forward and reverse IV curves of the champion H3pp:HP PSC.* **c-d,** *PCE and V_{oc} statistics of the reference (HP) PSCs (blue) and the H3pp:HP-based PSCs (orange). The boxes show the 25th and 75th percentiles, and the whiskers display the 5th and 95th percentiles. The median and mean are indicated by the dividing lines across the boxes and the open square symbols, respectively. The maximum and minimum values are represented by the cross*

*symbols. **e,** TRPL for the HP (blue) and the 1:500 H3pp:HP ratio (orange) on glass. **f,** OPTP for the HP (blue) and the 1:500 H3pp:HP ratio (orange) on glass.*

To understand whether the recombination behaviour of the photoexcited carriers unequivocally comes from the perovskite films, **TRPL** analyses were carried out on HP thin films (deposited on glass) with and without the H3pp molecule. **Figure 1e** shows the TRPL decay of reference and optimized H3pp:HP (1:500 ratio) films were measured at a low fluence (509 nm, 50 nJ/cm^2 per pulse, equivalent to ~1 sun). The monoexponential fits to the data result in characteristic lifetimes very similar for both samples of $\tau \approx 230$ ns.[42, 42] The charge carrier lifetime is strongly related to the defect/trap density of the material under study, especially the nonradiative recombination.[42] The PLQE at 1 sun reached values of 1.90 % and 1.94 % for the HP and HP:H3pp thin films, respectively, demonstrating the good quality of the films and corroborating the similar recombination process in both samples (**Table S1**). TRPL measurements at higher light intensities (fluences) equivalent to 1, 5, 10 and 100 suns **(Figure S7)** indicate very similar responses for the samples with and without the H3pp molecule up to 5 suns **(Figure S7a-b**). The similar charge carrier lifetimes at low fluences indicate that the addition of the H3pp molecule does not reduce nonradiative recombination in the perovskite films. However, for higher light intensities, i.e., 10 and 100 suns, we observed longer lifetimes, which could indicate a slight reduction in nonradiative recombination for the sample treated with H3pp in comparison to the neat HP films (**Figure S7c-d**). The comparable nonradiative recombination observed for the thin films with and without H3pp addition is supported by the comparable PLQEs and estimated quasi-Fermi level splitting values (QFLS, upper limit for V_{oc}) in the perovskite films and PSCs (**Table S1-a and S1-b, respectively**).[43,44,45] Furthermore, we have also extracted the trap density of perovskite thin films with and without the addition of the H3pp additive from space-charge-limited current (SCLC) measurements (**Figure S8**). Results show that the electron and hole trap density do not change significantly when the H3pp is added, in line with the TRPL and PLQE results.

To probe the carrier dynamics on a shorter time scale, we employed OPTP spectroscopy with subpicosecond temporal resolution. In this experiment, we probed light-induced changes in the conductivity – i.e., the photoconductivity – as a function of the pump-probe delay time.[46] We carried out measurements on the structure of silica glass/perovskite for both the reference HP and the HP:H3pp sample (**Figure 1f**). We observed that within a few picoseconds after excitation with the pump pulse (15 μJ/cm^2, 800 nm), the photoconductivity is positive, indicating the presence of light-induced mobile charges. We observe a second-order recombination process caused by nongeminate electron-hole pair recombination,[47] leading to a reduction in the photoconductivity that is observable within a nanosecond. This process is followed by relaxation on a timescale of many nanoseconds (as

probed using TRPL), which manifests as a constant long-term background in the background conductivity in the short OPTP time window (see also **Figure S8**). We also observe that the normalized dynamics are nearly identical for the samples regardless of the presence of the H3pp additive.

In summary, our results show very similar values of V_{oc} and PCE (**Figure 1 and Figure S5**) for the PSCs regardless of the presence of H3pp, which is ascribed to the negligible impact of H3pp on the nonradiative recombination of the HP and devices at low fluences (1 sun). Slight differences in the optoelectronic properties (longer lifetimes) of the H3pp:HP thin film are observed only at higher fluences (**Figure S7-S9**); however, these values are not convincing enough to firmly state that the addition of H3pp reduces nonradiative recombination. Given that the nonradiative recombination is closely related to deep level defects that act as recombination centres, we speculate that defects (especially deep defects) are not passivated or that their passivation is negligible in our thin films when the H3pp additive is employed.

Device stability and ion immobilization

We sought to evaluate any possible effect of H3pp on the operational stability and ion migration of the PSCs (**Figure 2a**). For this purpose, we followed the ISOS protocols recently reported for PSCs under 1 sun continuous illumination for 1000 h in N_2 (ISOS-L-1I).[19] First, we carried out stability analysis on the reference PSCs employing as the absorber the RbCsMAFA (●), without additive (blue) and PSCs with an optimal H3pp:HP ratio of 1:500 (orange) (**Figure 2a**). The PSC with the optimal 1:500 H3pp:HP ratio retained nearly 100 % of the initial PCE, while the stability observed for the reference PSC showed about 28 % performance loss after 1,000 h under the same operational conditions (**Figure 2a**). Notably, we replicate the same trends in other perovskite compositions such as $Cs_{0.05}MA_{0.15}FA_{0.80}Pb_{1.05}(I_{0.85}Br_{0.15})_3$ (CsMAFA) (**Figure 2a**, ■, and **Figure S10**). The main difference between PSCs with the two HP is the initial few hours of the stability analyses for the PSC with the CsMAFA, where a decrease in PCE is initially observed and stabilizes with time. This response has been observed before and is attributed to the charge accumulation at the interface with Spiro-OMeTAD[34,48]. Interestingly, our results demonstrate that the addition of H3pp can be extended to different HP absorbers with similar long-term stability results. We also evaluate the effect of the additive on the PSCs response at higher temperatures through the study of thermal stability analyses. The experiments were made in un-encapsulated PSCs with and without the addition of the H3pp (1:500) in a N_2–filled glove box at 65 $^{\circ}$C. **Figure S11** shows that after aging for 120 h, the device containing the H3pp additive retained over 80% of its original PCE while the reference sample only less than 70% of its original efficiency. This result demonstrates that H3pp can improve the thermal stability of PSCs.

To further understand the outstanding stability of the PSCs when we apply the H3pp molecule, we performed **OPTP, PLQE** and **TRPL** measurements on the perovskite films with and without H3pp on glass over time at high light intensities (**Figure 2b and c**). The use of a high light intensity has been proposed as a way to accelerate the degradation of PSCs and to predict the solar cell lifetime since high intensity illumination of several suns can tremendously accelerate the degradation of solar cell devices and materials.[19] **Figure 2b** shows the OPTP measurements of the photoconductivity carried out on the reference HP and H3pp:HP thin films under 4 suns for 10 h. Data were taken every 30 min. The results indicate that the sample with the H3pp additive exhibits a more stable and higher photoconductivity after 2 h of light irradiation compared with the reference sample, which shows a slow but steady decrease in the photoconductivity. The THz photoconductivity is proportional to the number of photoexcited electron-hole pairs and to the mobility of these charges. Thus it provides microscopic insights into the fundamental processes (charge creation and charge transport) of the solar cell. The long-term stability of this signal demonstrates that the same number of charges is created and their mobility stays constant. The monitored response of the steady-state photoluminescence (PL) peak intensity under continuous irradiation of 100 suns for ~10 min (500 sec) under a N_2 atmosphere (**Figure 2c**) also demonstrates the high stability of the HP with H3pp in comparison with the reference HP, which degrades almost immediately after only a few seconds.
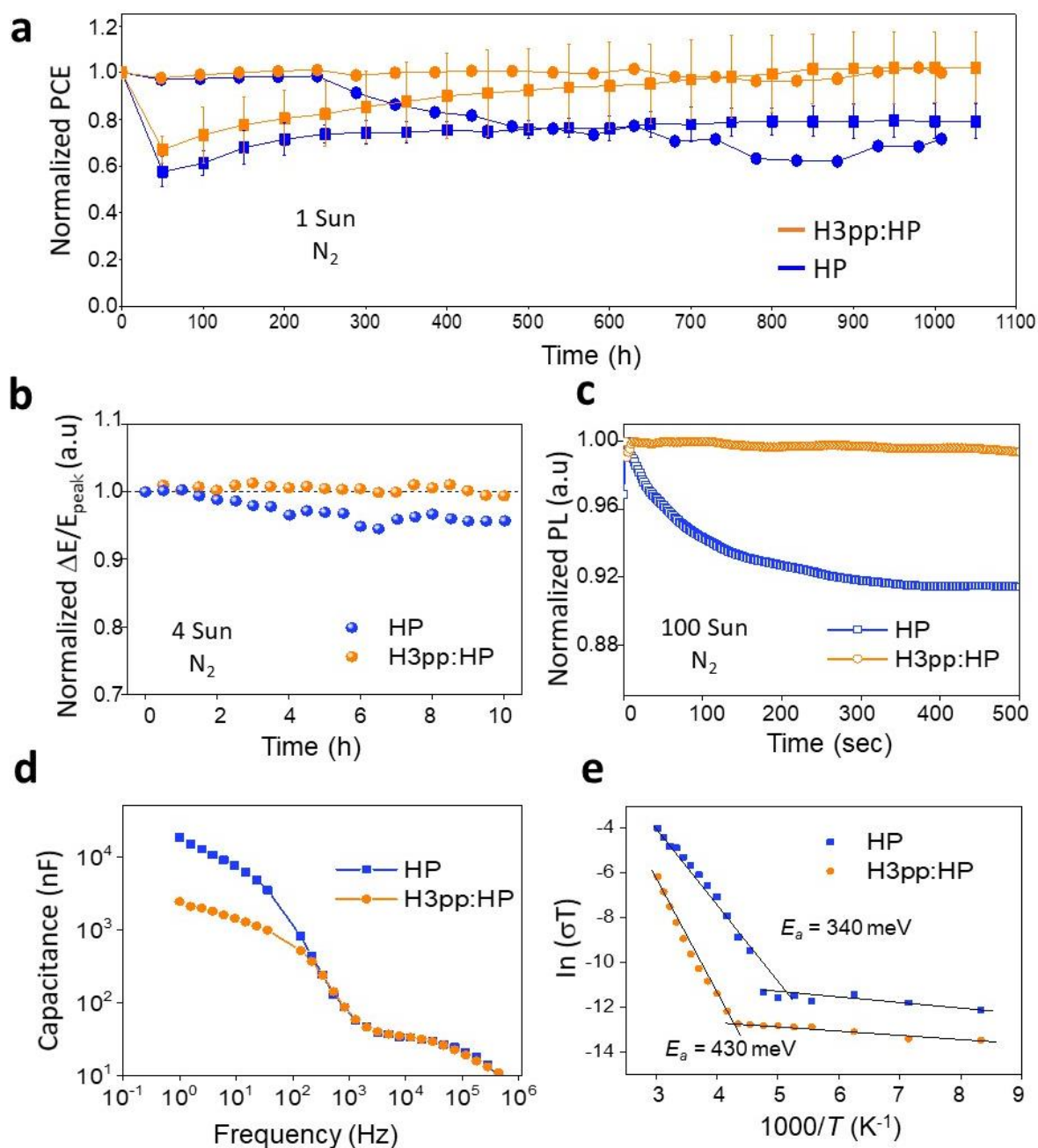
Figure 2. Device stability and ion immobilization. a, *Operational stability of PSCs applying RbCsMAFA (●) and CsMAFA (■) with only HP (blue) and with the H3pp:HP (orange), under 1,000 h of continuous illumination at 1 sun under a N$_2$ atmosphere using white LEDs and MPP tracking.* ***b,*** *OPTP analyses of perovskite films on glass, carried out in N$_2$ under 4 suns for 10 h.* ***c,*** *PL measurements carried out on perovskite films on glass in N$_2$ under 100 suns for 500 sec.* ***d,*** *Frequency-dependent capacitance of PSCs under 1 sun.* ***e,*** *Temperature-dependent dark conductivity of HP thin films on glass.*

To analyse the role of ion migration in the samples, we applied electrochemical impedance spectroscopy (EIS) and temperature-dependent dark conductivity measurements to PSC samples and HP thin films, respectively. **Figure 2d** shows the frequency-dependent capacitance of the PSCs with

and without the H3pp additive obtained from the Nyquist plot of the EIS spectrum. The capacitance in the low frequency range (1-100 Hz) is one order of magnitude lower for the device with the H3pp molecule, indicating an effective reduction in ion migration and charge accumulation at the interfaces[29]. Ion migration activation energy (E_a) analysis was performed on HP samples deposited on glass via temperature-dependent dark conductivity measurements (**Figure 2e**) according to the Nernst–Einstein relation of $\sigma(T) = \sigma_0/T^* \exp(-E_a/kT)$, where T is the temperature, k is the Boltzmann constant, σ_0 is a constant, and the activation energy E_a can be extracted from the slope of the $\ln(\sigma T) \sim 1/KT$ relation. The E_a for the HP is 340 meV, while 430 meV is obtained for the sample with the H3pp molecule, indicating effective mitigation of ion migration.

In summary, the addition of H3pp has no substantial beneficial effect on the efficiency for PSCs under equilibrium conditions (as-prepared). Notably, it brings remarkable long-term stability to the PSCs analysed under nonequilibrium operational conditions (continuous light irradiation). Analyses of the carrier recombination and photoconductivity under multi-sun illumination support the high stability observed with the use of the H3pp additive not only under 1 sun but also under severe light irradiation up to 100 suns. Our results also demonstrate that the good stability can be extended to different HP absorbers, in this case CsMAFA anf RbCsMAFA. PLQE and OPTP analyses at low fluences (~1 sun) rule out any variation in the non-radiative defect concentration. However, analyses at increasing fluences (above 10 suns) result in a small decrease in the deep trap density, which has an enormous impact on the device stability but not on the device performance. Our results also demonstrate that ion immobilization is the mechanism behind the outstanding long-term stability of the PSCs when the H3pp additive is employed.

Effect of H3pp on the perovskite thin film: microstructure and binding mode

On the basis of the PV results and outstanding PV stability, we aim to understand the effect of the H3pp molecule on the morphology, structure and composition of the HP thin films. **Figure 3a** shows the morphology of the HP thin films with and without the H3pp additive in top-view SEM images. The addition of H3pp did not promote grain growth in the HP thin films since very similar grain dimensions (~280 nm on average) are observed for both samples. This indicates that grain boundaries are not reduced upon the addition of H3pp, in agreement with the similar nonradiative recombination levels in both types of PSCs, as grain boundaries are reported to be the source of defects[33,49]. **Figure 3b** shows a cross-sectional annular dark-field scanning transmission electron microscopy (ADF-STEM) image of the different layers of the PSC, where the selected area highlighted by a blue rectangle is the absorber HP:H3pp layer with a grain boundary. Electron energy loss spectroscopy (EELS) was applied to obtain

the chemical composition maps of the HP:H3pp layer. According to the EELS maps, phosphorus (from the −PO(OH)$_2$ of H3pp) is present in the HP bulk and is slightly richer near the grain boundary, demonstrating that H3pp is relatively segregated. As will be discussed later, X-ray diffraction (XRD) and solid-state nuclear magnetic resonance (NMR) confirm that H3pp is not incorporated into the crystal lattice. The cross-sectional lamella may contain several grains in the electron beam direction, and when the surface of the grains is surrounded by H3pp (at the 3D level), the EELS maps will show phosphorus in the bulk and a slightly rich presence at grain boundaries.

The XRD patterns of the RbCsMAFA perovskite thin films without H3pp and at the optimal H3pp:HP 1:500 ratio are shown in **Figure 3c**. No new peaks or peak shifts are observed in any of the HP films with different H3pp concentrations (**Figure S12**), indicating that H3pp may not be incorporated into the perovskite crystal lattice. Further solid-state NMR studies confirm that H3pp is not incorporated into the crystal lattice and most likely resides in the grain boundaries and on the surfaces (**Figure S13**). This is also supported by the nearly unchanged band gap (~ 1.56 eV) deduced from PL and UV-vis spectra obtained upon the addition of H3pp (**Figure S14**). The (-111) crystal plane for the H3pp-doped sample is enhanced in comparison with the reference sample (**Figure 3c**). The impact of the crystal orientation on the PSC performance is currently under debate by the research community[15,50], probably due to variations in the precursor composition and fabrication processes. In our case, a negligible influence is observed.

Evidence of the interaction between H3pp and the HP is found with FTIR analysis (**Figure 3d**). The peak at 1712 cm^{-1} corresponds to the antisymmetric C-N stretching (overlapping with the C=O stretching), and the peak at 1470 cm^{-1} corresponds to the symmetric NH$_3^+$ bending. After the introduction of the H3pp molecule into the HP layer, the stretching vibration of −P=O in H3pp shifts from 1268 cm^{-1} to 1243 cm^{-1}, whereas that of −C=O remains almost unchanged (1710 cm^{-1} to 1708 cm^{-1}), which indicates a strong interaction of H3pp with the HP through the phosphonate group and a weak interaction through the carboxylate group.
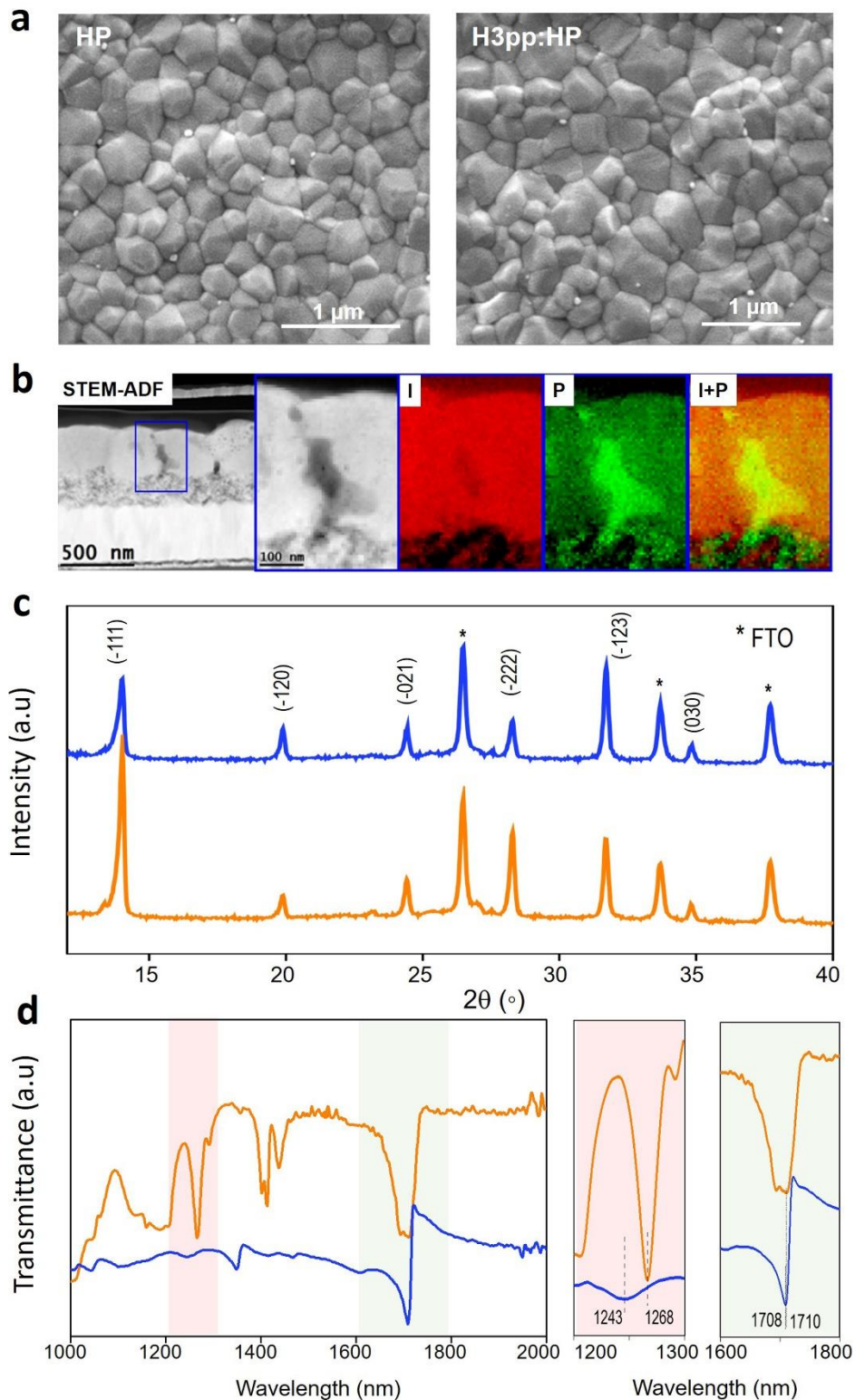
Figure 3. Effect of H3pp on the perovskite thin film: microstructure and binding mode. *Comparison of the microstructural analysis of the RbCsMAFA (blue) and H3pp:RbCsMAFA 1:500 ratio (orange) thin films: **a,** Top-view SEM image. **b,** ADF-STEM micrograph (lateral view) of the HP:H3pp 1:500 ratio PSC, and corresponding EELS chemical composition maps of the selected absorber region with a grain boundary (blue rectangle): Individual I (red), P (green) and I + P. The L-edge (132 eV) was applied for the P analysis in the elemental maps. **c,** XRD patterns. **d,** FTIR analysis of the HP (blue) and HP:H3pp (orange), indicating the peaks corresponding to the P=O stretching mode between 1220 and 1300 nm and the C=O stretching mode between 1600 and 1800 nm.*

To obtain more atomistic information regarding the interaction mode of H3pp with the HP, we further investigated their interaction by using DFT. We chose α-FAPbI$_3$ as a simple perovskite model (FA is the dominant cation in the perovskite applied in this work). We began by computing the binding energy ($E_{binding}$) of the H3pp molecule at FAI- and PbI$_2$-terminated FAPbI$_3$ surfaces as $E_{binding} = E_{H3pp} + E_{surface} - E_{surface-H3pp}$, where $E_{surface-H3pp}$, E_{H3pp} and $E_{surface}$ are the total energies of the H3pp-FAPbI$_3$ system, H3pp molecule and FAPbI$_3$ surface, respectively. We considered a number of possible interaction modes between the two, including the interaction of O-FA, H-I, and O-Pb, where the first and second atomic species come from H3pp and the HP, respectively. All interaction modes are energetically favourable, with sizeable binding energies in the range of 1.6 eV to 3.1 eV (**Figure S15 and Table S2**). Notably, H3pp tends to bind much more strongly to the FAI-terminated surfaces than to the PbI$_2$-terminated surfaces, with all configurations having binding energies as high as 2.9 eV to approximately 3.1 eV.

Figure 4a shows the most favourable configuration (binding energy of 3.13 eV), where H3pp interacts with the HP such that –PO(OH)$_2$ points towards a FAI-terminated perovskite surface and forms a total of three hydrogen bonds of two different types. In the first type of hydrogen bond, the hydrogen atom from –P-OH interacts with I$^-$ (H-I), and in the second type, the oxygen atom from –P=O interacts with two hydrogen atoms from one NH$_2$ moiety of FA$^+$ (O-H). From a charge density difference analysis (**Figure 4b**), we observe that both types of hydrogen bonds are present due to a significant depletion of electrons from the H atoms to the O and I atoms. Because the involved H atoms come from both H3pp and the HP, significant charge redistribution occurs on both sides, confirming strong interface interactions. Because of the newly created hydrogen bonds with the perovskite, we expect a slight weakening of the P=O bond itself in H3pp. Indeed, the wavenumber of the stretching mode of the –P=O bond, as calculated by DFT, shifts from 1246 cm^{-1} to 1171 cm^{-1} (**Figure 4c**), which is a sign of weakening of the bond. Note that we also find another similar strong interaction mode of –PO(OH)$_2$ with the FAI-terminated perovskite surface, a second favourable configuration with a binding energy of 2.99 eV (**Figure S15b** and **Table S2**), where only two hydrogen bonds (instead of the three in **Figure S15a** and **Figure 4a**) are formed. The calculated wavenumber of the stretching mode -P=O for this structure also shifts to a lower wavenumber of 1207 cm^{-1}. While the wavenumber of the stretching mode of the -P=O bond shift to lower wavenumbers, that of the -C=O stretching mode remains almost unchanged (**Figure 4c**), indicating the absence of a strong interaction with the HP. Our experimental FTIR spectrum shown in **Figure 3d** confirms both trends. Therefore, combining the DFT calculations and FTIR data, we can establish that the dominant mode of interaction between the H3pp molecule and the perovskite is through the formation of two types of hydrogen bonds between the –PO(OH)$_2$ moiety and the FA$^+$ cations and I$^-$ anions. This is further supported by additional XPS, FTIR, XRD and Liquid-state ^{1}H NMR measurements carried out to the samples, as shown in **Figure S16 and S17.**
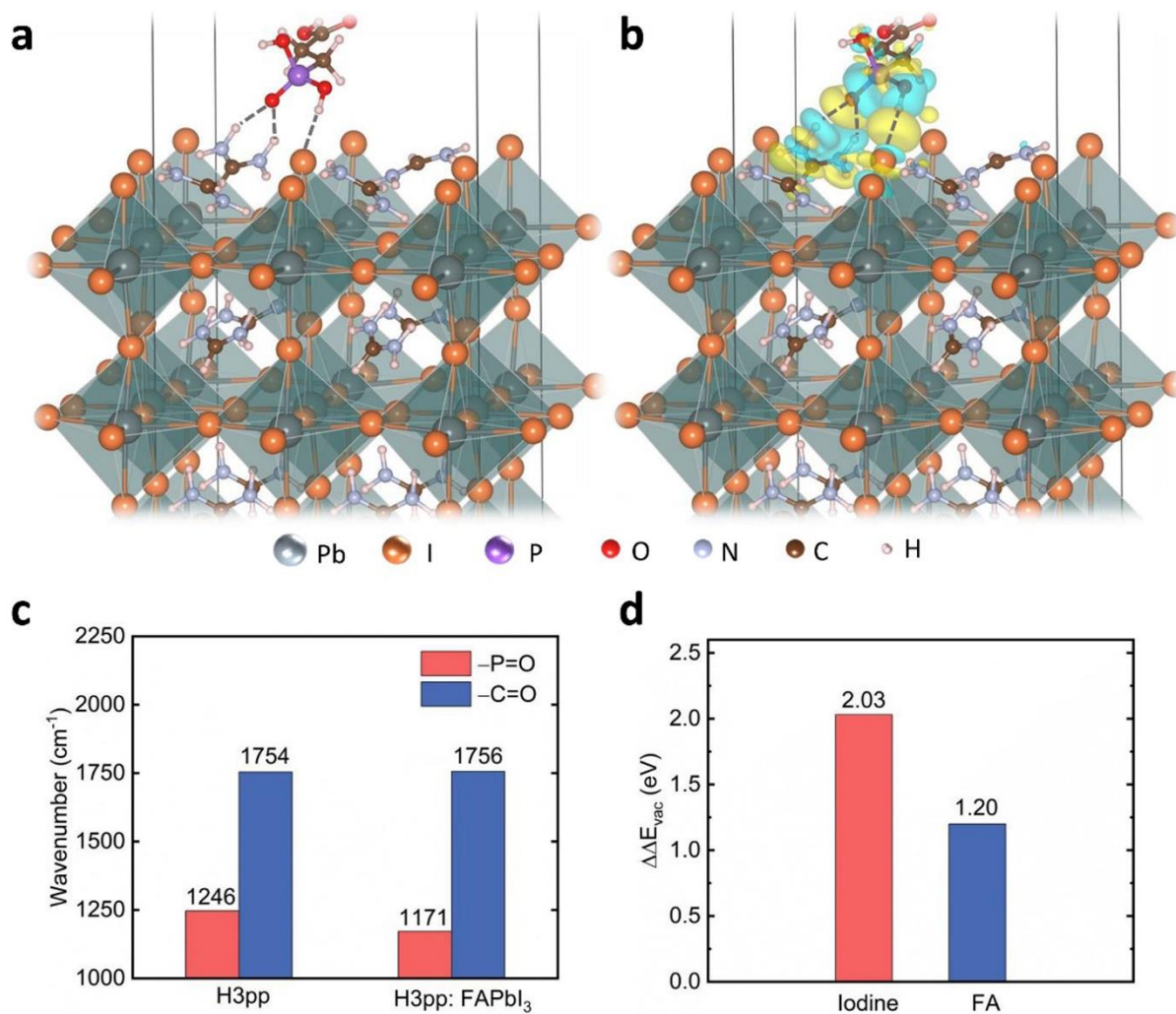
Figure 4. Theoretical analysis of the interaction modes between H3pp and FAPbI₃. a, *Example of one dominant interaction mode, where H3pp binds to the FAI-terminated surface of FAPbI₃, forming three hydrogen bonds of two different types.* ***b,*** *Charge redistribution at the H3pp/FAPbI₃ interface upon the adsorption of H3pp, where charge accumulation and depletion are indicated by yellow and cyan, respectively.* ***c,*** *Calculated FTIR wavenumbers of the stretching modes of the −C=O and −P=O bonds for H3pp and H3pp-modified FAPbI₃.* ***d,*** *Formation energy of surface FA and I vacancies in H3pp-modified FAPbI₃ compared with reference FAPbI₃.*

Having established the dominant interaction modes of H3pp with the HP surface, we continue to study the effect of such interactions by calculating the formation energies of I anion and FA cation vacancies on the surface of the clean perovskite and on a surface that incorporates H3pp. As shown in **Figure 4d**, the I and FA vacancy formation energies for a perovskite surface coordinated with H3pp species are increased by 2.03 and 1.20 eV, respectively, compared to the pristine perovskite. The second favourable configuration also gives slightly smaller (compared with the most favourable configuration) but still significantly large defect formation energy differences of 1.99 eV (for I vacancies) and 0.84 eV (for FA vacancies) compared with the pristine HP. The presence of H3pp therefore inhibits the formation of I and FA vacancies at the surface. This result illustrates the mechanism behind ion immobilization and supports the excellent operational stability of the H3pp-modified PSC (**Figure 2a**),

where the creation of I and organic cation vacancies is typically believed to be responsible for the migration of ions in the perovskites under operational stress, such as electrical bias and light excitation[51].

In brief, the incorporation of H3pp within the HP layer leads to high nanostructure quality as a thin film absorber but does not translate into large grain sizes of the H3pp:HP thin film. The strong interaction between the HP and H3pp is corroborated by FTIR and NMR analyses. Our combined experiments and DFT analysis point to a strong interaction of the H3pp species with the perovskite surface, particularly via the phosphonate group. Such strong interactions include two types of hydrogen bonds (H-I and O-H). All these interactions potentially prevent the creation and diffusion of several point defects (e.g., FA and I vacancies) at the surfaces and grain boundaries of the perovskite film, enabling ion immobilization and highly stable PSCs under operational conditions.

Passivation of shallow point defects in the HP absorber

The current understanding of point defects in PSCs indicates that passivation of deep defects (e.g., Pb-I antisite defects)[14] reduces the nonradiative losses and has a direct impact on the device performance (V_{oc} and efficiency)[3-5]. In our work, the PLQE and OPTP results at low fluences (~1 sun) rule out any variation in the non-radiative defect concentration. However, analyses at increasing fluences (above 10 suns) indicate a small decrease in the deep trap density, which has an enormous impact on the device stability but not on the device performance. This result is unexpected because the application of additives in high-quality PSCs usually enhances both the efficiency and stability, and the role of defects in these properties is often linked. However, HPs are ionic-electronic conductors and posses a strong component of charged shallow level traps which are not often considered. Our work, suggests that the strong binding modes of H3pp with the phosphonate functional group passivate defects through shallow point defects (e.g., FA and I vacancies)[30,31] that block or immobilize ions (for example, MA, FA or I). To demonstrate that the passivation of shallow point defects is taking place in our samples, we carried out thermal admittance spectroscopy (TAS) measurements[15] under various temperatures with the aim of studying the energetic distribution of defects in the PSCs. As is shown in **Figure 5**, the HP reference devices (without the H3pp additive) mainly have two types of shallower defects centered at ~0.13 eV (D1) and ~0.16 eV (D2), while the H3pp:HP devices have only one type of deeper defect at ~0.20 eV (D3). The absence of shallower defects (D1) in the H3pp:HP devices and the comparable concentration of the deeper defects in all devices (D2 and D3) imply that the addition of H3pp can indeed passivate the shallow defect D1 and impacts less on the deeper defect D2.

Recnt work by Prof. Yang's group suggests that shallow traps are generated at the surface of the halide perovskite grains due to different post-treatments[7]. To verify if this can also happen in our samples, we carried out a post-treatment study where the H3pp (in isopropanol) was deposited as a thin layer on top of a halide perovskite film. The resulting films were employed to fabricate PSCs and analyzed their operational stability under illumination. **Figure S18** shows indeed that the surface treatment results in devices of comparable PCE and also improved operational stability for the samples with the H3pp in comparison with the reference device. Although the stability is not as good as the one obtained by adding the H3pp into the halide perovskite precursor solution (as reported in this manuscript), these results demonstrate that the H3pp additive can also passivate the surface defects and improve the device stability.
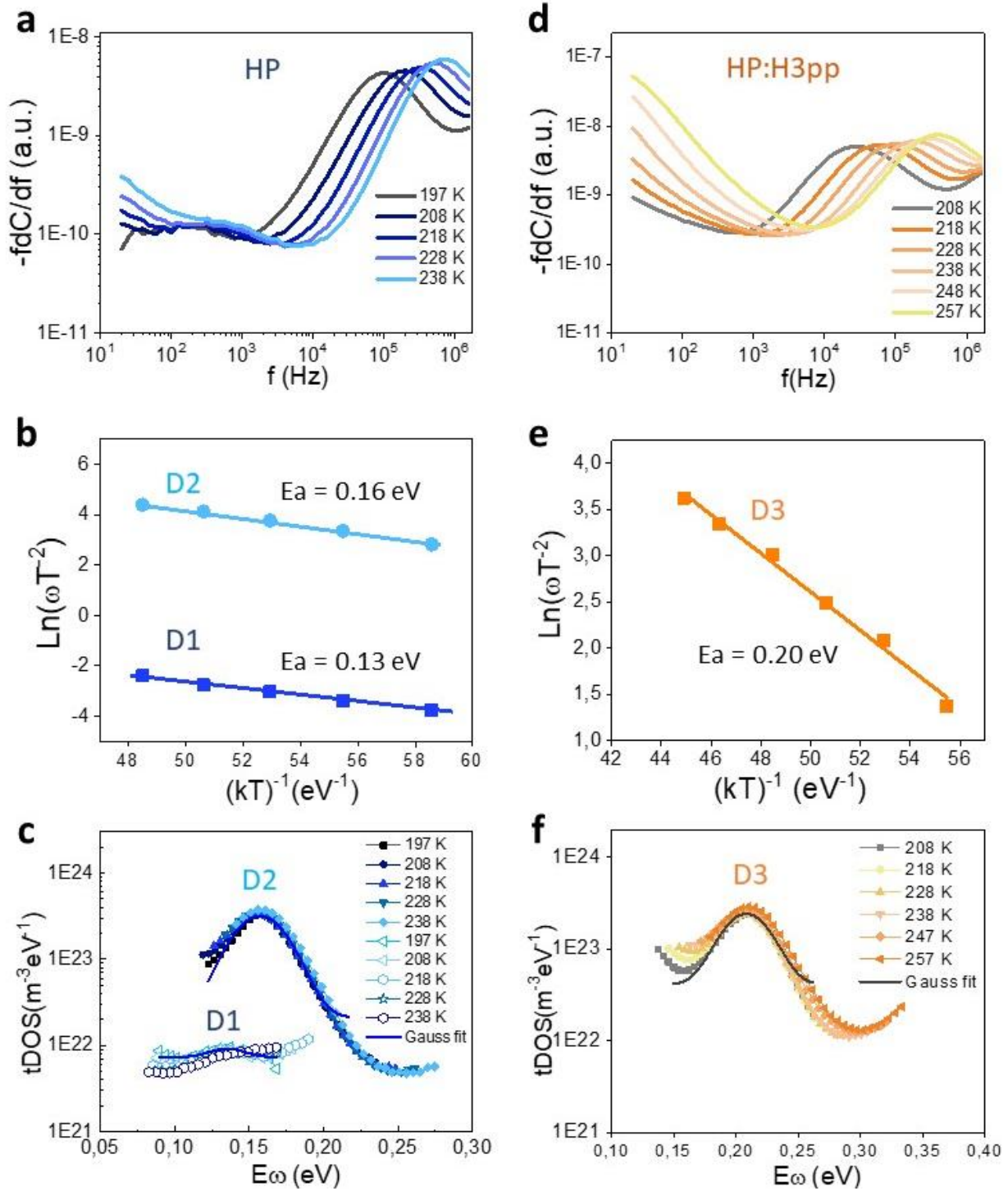
Figure 5. Passivation of shallow point defects in the HP absorber. *Differentiated capacitance spectra (a, d), Arrhenius plots of the inflection frequencies determined from the derivative of the admittance spectra (b, e) and trap density of states (tDOS) deduced from temperature-dependent C–f plots (c, f) for the perovskite solar cells with (d-f) and without H3pp (a-c). The activation energy (Eₐ) was extracted for each defect and shown inside the figures.*

In brief, we have demonstrated that adding the H3pp additive to the halide perovskite absorber results in similar concentration of deep defects and the reduction or passivation of shallow point defects. This explains the similar photovoltaic response for the PSC with or without the addition of the H3pp additive since deep defect affects efficiency and voltage. It also demonstrates that the H3pp passivates shallow defects through hydrogen bonding with the perovskite, reducing ion movment and enhancing the PSC long-term stability. We expect that our results will permit to increase the understanding between defect passivation and PSC operational stability: It is not only significant to passivate defects responsible for deep level traps, it is also important to consider defect-induced shallow level traps. Finally, the relation of defect passivation and ion immobilization in these additives is not a simple task. The effect of multiple aspects are usually taking place simultaneously on the stability enhancement process. For example, intrinsic factors such as the concentration, size and structure of the additive (as shown in **Figure S1**), as well as extrinsic factors such as high temperature, humidity or electrical bias shoud also be part of future studies.

Conclusions

In summary, by applying the H3pp molecule to the perovskite precursor solution, we fabricated solar cells with excellent optoelectronic properties (V_{oc} of ~1.1 V and PCE of ~21 %), which are not affected by the H3pp additive. Remarkably, the PSCs display outstanding operational stability, retaining nearly 100 % of the initial PCE after 1000 h under MPP operational conditions and light irradiation. The H3pp additive strongly bonds to the perovskite through the $-PO(OH)_2$ functional group via two types of hydrogen bonds (H···I and O···H), passivating shallow point defects (e.g., FA and I vacancies). Since the passivation does not occur through deep defects (e.g., Pb-I antisite defects), the nonradiative recombination is not mitigated, and the device performance (V_{oc} and efficiency) remains unaffected by the presence of the H3pp additive. Such binding modes facilitate immobilization of halide anions and organic cations, blocking ion migration and improving the device stability. Our findings permit decoupling of the effects of defects on the stability and performance and advance on the understanding of the relation between shallow and deep defect passivation, non-radiative recombination and PSC stability. A further understanding of the nature of the different binding modes of the functional groups of additives in HPs will likely be essential for the development of stable operational PSCs.

EXPERIMENTAL PROCEDURES

Resource Availability.
Lead Contact
Further information and requests for resources and materials should be directed to and will be fulfilled by the Lead Contact, Monica Lira-Cantu (monica.lira@icn2.cat).

Materials Availability
This study did not generate new unique materials.

Data and Code Availability
The published article includes all data analyzed and necessary to draw the conclusions of this study in the figures and tables of the main text or Supplemental Information. Further information and requests should be directed to the Lead Contact.

Chemicals. PbI_2 (TCI, >98%), $PbBr_2$ (TCI, >98%), FAI (Greatcell), MAI (Greatcell), MABr (Greatcell), CsI (ABCR, 99.998%), RbI (ABCR, 99.998%), dimethylformamide (DMF) (ACROS organics, 99.8%, extra dry), dimethyl sulfoxide (DMSO) (ACROS organics, 99.8%, extra dry), 2,2',7,7'-tetrakis(N,N-di-p-methoxyphenyl-amine)9,9'-spirobifluorene (spriro-OMeTAD) (Merck), 4-tert-butylpyridine (TBP) (Sigma Aldrich), lithium bis(trifluoromethanesulfonyl)imide (Li-TFSI) (Sigma Aldrich), titanium diisopropoxide bis(acetylacetonate) (Sigma Aldrich), acetylacetone (Sigma Aldrich), titania paste (Greatcell), chlorobenzene (Sigma Aldrich), 3-phosphonopropionic acid (Sigma Aldrich), acetonitrile (Sigma Aldrich).

Device fabrication. FTO substrates (Nippon Sheet Glass 10 Ω/sq) were etched by Zn powder and 4M HCl, and then were cleaned with Hellmanex®, acetone and ethanol for 15 min, respectively inside an ultrasonic bath, finally were immediately dried with dry air. Compact TiO_2 (c-TiO_2) solution was prepared with titanium diisopropoxide bis(acetylacetonate): acetylacetone: ethanol = 0.6: 0.4: 9 (v : v) and then were sprayed onto FTO substrates at 450 °C.Mesoporous TiO_2(m-TiO_2) paste was prepared with titanium paste: ethanol=1:6 (w:w), and was spin coated to c-TiO_2 substrates at 5000 rpm for 20s and then annealed at 450 °C for 30 min. After that, the as-prepared FTO/c-TiO_2/m-TiO_2 substrates were quickly transferred to a N_2 filled glove box for perovskite and spiro-OMeTAD deposition (no post-treatments were conducted for the substrates before deposition). The quadruple cation halide perovskite $Rb_{0.05}Cs_{0.05}MA_{0.15}FA_{0.75}Pb_{1.05}(I_{0.95}Br_{0.05})_3$ was prepared as follows. Briefly, first 1.5 M stock solution of 1) CsI (DMSO), 2) RbI (DMSO), and 3) PbI_2 (DMSO:DMF=1:4) were prepared, respectively. Then 1.5 M 4) $(MABr)_{0.9}(PbI_2)$ (DMSO:DMF=1:4), and 5) $(FAI)_{0.9}(PbI_2)$ (DMSO:DMF=1:4) were freshly prepared by dissolving MABr or FAI power in solution 3), respectively. After that, the solutions were mixed at a ratio of 4) : 5) : 1) : 2) : 3) = 190 : 950 : 60 : 60 : 60 (v:v) in sequence. The triple cation halide perovskite $Cs_{0.05}MA_{0.15}FA_{0.80}Pb_{1.05}(I_{0.85}Br_{0.15})_3$ was prepared as follows. Briefly, first 1.5 M stock solution of 1) CsI (DMSO), 2) $PbBr_2$ (DMSO:DMF=1:4) and 3) PbI_2 (DMSO:DMF=1:4) were prepared, respectively. Then 1.5 M 4) $(MABr)(PbBr_2)$ (DMSO:DMF=1:4) and 5) $(FAI)(PbI_2)$ (DMSO:DMF=1:4) were freshly prepared by dissolving MABr or FAI power in solution 2) and solution 3), respectively. After that, the solutions were mixed at a ratio of 4) : 5) : 1) : 3) = 150 : 800 : 50 : 100 (v:v) in sequence. 3-phosphonopropionic acid (H3pp) doped perovskite solutions were prepared by simply dissolving H3pp in the perovskite precursor solution to achieve H3pp: perovskite with various molar ratios (no heat or stirring is needed). The perovskite spin coating process was carried out at 2000 rpm for 10s, and then 6000 rpm for 30s. Initially, 50 µL perovskite solution was dropped on a 1.5*2.5 cm^2 FTO/c-TiO_2/m-TiO_2 substrate. During the second step of spin coating, 100 µL chlorobenzene was dropped at 15s before ending. The samples were annealed at 100 °C for 1 h on a hot plate for crystallization. Hole transporting layer was prepared by dissolving 0.12 g spiro-OMeTAD in 1130 µL chlorobenzene and then doped with 47.3 µL TBP and 23.5 µL Li-TFSI (1.8 M in acetonitrile). The spin coating was conducted at 4000 rpm for 20s with 50 µL solution. The finished devices were placed inside a dry air box for 12

hours to fully oxidize the spiro-OMeTAD. Finally, 80 nm Au was deposited as the front electrode by thermal evaporation. The evaporation rate was controlled in different stages to limit the damage to the spiro-OMeTAD layer: 0.003 nm/s for 0 - 1nm, 0.01 nm/s for 1- 10 nm, 0.02 nm/s for 10 - 20 nm and 0.06 nm/s for 20 - 80 nm.

Solar cell characterization. The solar cells IV curves were measured using a 450 W Xenon light source (Oriel) equipped with an arc lamp housing (Newport, Model 66902, 50-500 W). The light intensity was calibrated with a Si photodiode equipped with an infrared cutoff filter (KG3, Schott), and was recorded during each measurement. I-V curves of the cells were obtained by a digital source meter (Keithley 2400). The voltage scan rate was 10 mV/s. The cells were masked to get 0.16 cm^2 active area. Incident photon-to-electron conversion efficiency (IPCE) measurements were made based on a commercial apparatus (Arkeo-Ariadne from Cicci Research) using a 300 W Xenon lamp. All the measurements were conducted in air at room temperature.

Solid-state NMR measurements. Starting materials were stored inside a glove box under argon. Perovskite powders were synthesized by grinding the reactants in an electric ball mill (Retsch Ball Mill MM-200 using a grinding jar (10 ml) and a ball ($\varnothing$10 mm) for 30 min at 25 Hz. The resulting powders were annealed at 140 °C for 10 minutes to reproduce the thin-film synthetic procedure. The amounts of reagents taken into the synthesis were as follows:
α-FAPbI$_3$: 0.172 g formamidinium hydroiodide (1.00 mmol) and 0.461 g PbI$_2$ (1.00 mmol).
H3pp-doped α-FAPbI$_3$ (1:25 mol/mol): 0.172 g formamidinium hydroiodide (1.00 mmol), 0.461 g PbI$_2$ (1.00 mmol), and 0.006 g (0.04 mmol) H3pp.
^{14}N (65.0 MHz) and ^{31}P (364.4 MHz) NMR spectra were recorded on a Bruker Avance Neo 21.1 T spectrometer equipped with a 3.2 mm low-temperature CPMAS probe. ^{31}P chemical shifts were referenced to 85% phosphoric acid. ^{14}N spectra were referenced to solid NH$_4$Cl (0 ppm) at 298 K. Low-temperature ^{1}H-^{31}P cross-polarization (CP) experiments used 1 ms optimized contact pulses, 4 s recycle delay, and 63 kHz SPINAL-64 ^{1}H decoupling. Echo-detected ^{31}P spectra used the following optimized recycle delays: 1 s (α-FAPbI$_3$ doped with H3pp), 300 s (neat H3pp). ^{14}N spectra were acquired with recycle delays of 0.1 and 0.5 s, respectively.

Fourier transform infrared spectroscopy (FTIR). FTIR was obtained by using TENSOR 27 FT-IR spectrometer (Bruker). Perovskite and H3pp-doped perovskite thin film were prepared following the same process as the devices, and then were scratched off carefully and mixed with KBr for measurements. To increase the signal of FTIR, concentrated H3pp doping was applied (H3pp: perovskite = 1:2.5).

Electron energy loss spectroscopy (EELS). Focused ion beam (FIB, Zeiss Crossbeam 1560XB) was applied to prepare the lamellae for HRTEM measurements. 2 μm of Pt/carbon layer was deposited on top of the Au (active area) using electron beam evaporation to avoid the damage of the layer during FIB process. The initial cut for trenches was performed at 10 nA, then 2 nA and last polishing at 500 pA and 200 pA to limit the damage. Then the lamellae were lifted out and attached to the TEM grid. Final polishing was conducted in consecutive steps. The initial step was at 30 kV, 50 pA tilted at 57º (perpendicular to the FIB) and the final step was at 5 kV, 10 pA to avoid Ga$^+$ contamination as much as possible until the lamellae were transparent in the detector at 3 kV (electron acceleration voltage). The lamellae are around 50 - 100 nm. To limit the possible degradation in air, fast transfer of lamellae in and out of the system was conducted (< 2 min). A grounded bracelet was used to take out the lamellae grid to avoid electrostatic damage. EELS analyses were obtained by using a FEI Tecnai F20 field emission gun microscope operated at 200 kV, which is equipped with a high-angle annular dark field (HAADF) detectorand embedded Quantum Gatan Image Filter. Images have been analyzed by means of GatanDigital Micrograph software.

Scanning electron microscopy (SEM). SEM was performed using Quanta 650F with 5 kV accelerating voltage at a working distance of 8 cm.

X-ray diffraction (XRD). X-ray diffraction (XRD) of the sample was measured using Empyrean (Panalytical) equipped with a ceramic tube (Cu anode, λ = 1.54060 Å) and a PIXel[1D] (Panalytical) detector. XRD data was analyzed using HighScore Plus software.

Electrochemical Impedance Spectroscopy (EIS). Capacitance-Frequency measurements of perovskite solar cells were recorded with Paios (Fluxim, electrical measurement all-in-one platform for solar cells). The measurements are under a white LED source with calibrated light intensity close to one sun.

Time-resolved photoluminescence (TRPL), Photoluminescence quantum efficiency (PLQE) and steady-state photoluminescence (PL)., PLQE and PL measurements were conducted by placing the samples in an integrating sphere. The different films were photoexcited by a 532-nm continuous-wave laser. The laser power was set at 60 mW/cm^2 by using a calibrated power meter, and it was monitored over time to ensure reproducible conditions for all the samples. Laser signal, laser signal attenuated by the sample (absorption) and photoluminescence signal were collected by an optical fibre coupled to an Andor iDus Si Detector, with an accumulation time of 30 s for each measurement. The optical response of the integrating sphere, the optical fibre and the detector were calibrated. The protocol followed for measuring and calculating the PLQE is based on reference.[52] For TRPL, a 509 nm pulsed (1 MHz repetition rate) semiconductor laser was used for excitation. The average laser power was set at 60 mW/cm^2 (one sun equivalent intensity, or higher power equivalent to 5, 10 and 100 sun). A hybrid PMA photodiode with time resoloution of 25 ps was used as TCSPC detector. Samples were kept under N$_2$ atmosphere until characterised to prevent them from degradation.

Optical pump-THz probe (OPTP) spectroscopy. We perform photo-conductivity measurements of samples using optical pump-THz probe (OPTP) spectroscopy. In the setup, the THz generation is based on the optical rectification process in ZnTe non-linear crystals, using 800 nm pulses with duration of ~ 50 fs. The time-dependent electric field strength of THz pulses (~ 1-2 ps duration) transmitted the sample is detected by a second ZnTe crystal using electro-optic sampling. By fixing the sampling delay time to the peak position of the THz pulse, we monitor the THz absorption change by a third laser pulse with a wavelength of 800 nm. By tuning the time delay between the pump and THz probe, we measure the time-dependent THz absorption and therefore, the photo-conductivity of our sample in the time domain. The OPTP setup is kept in an N$_2$ environment to avoid THz absorption in air.

Temperature dependent dark conductivity. The conductivity of the perovskite with and without H3pp was measured at different temperatures by applying 2 V bias to glass/perovskite with electrode spacing of 10 μm on the surface, corresponding to an average electrical field of 0.2 V μm^{-1}. Sample temperature was varied in the close-circle He cryostat and measured by Si-diode from 120 K to 330 K. We firstly cooled the device to 120 K and then stabilized it at 120 K for half an hour. Subsequently the device was heated to an objective temperature with an interval of 20 K and stabilized at the temperature for 10 minutes before the current measurement was performed. To avoid transient current spikes which occurred in the first few seconds after bias, the conductivity was extracted from the device current between 20 and 50 s after the bias was applied.[53-55]

Light intensity dependent V$_{oc}$, Transient photocurrent (TPC) and Open circuit voltage decay (OCVD). Light intensity dependent V$_{oc}$, TPC and OCVD are analyzed at state-of-the-art devices (FTO/c-TiO$_2$/m-TiO$_2$/perovskite/spiro-OMeTAD/Au) using PAIOS (Fluxim, electrical measurement all-in-one platform for solar cells). The measurements are under a white LED source with varied light intensity from 0.3 to 1 sun for light intensity dependent V$_{oc}$[39] and 1 sun for TPC and OCVD.

Stability Analyses. The stability measurements were carried out following ISOS-L protocol for PSCs[19]. The tests were performed under N_2 atmosphere in a seald holder, tested under continuous light illumination and maximum power point tracking at room temperature (controlled and monitored to be 25 °C). The light source consisted of an array of white LEDs powered by a constant current. The LED type is LXM3-PW51 with an emission spectrum of 400-750 nm (see **Figure S19**). Equivalent sun intensities were calibrated using a calibrated Si reference diode equipped with a KG-5 filter.

Computational methods. Since FA as a cation and I as an anion are the most abundant species in the experimentally studied ($R_{0.05}Cs_{0.05}MA_{0.15}FA_{0.75}Pb_{1.05}(I_{0.95}Br_{0.05})_3$), the calculations were carried out using FAPbI$_3$ as a model system. The surfaces were modelled using slab models consisting of (2×2) cells in the x and y directions and nine atomic layers of iodine constructed from the bulk structure with a vacuum of 15 Å in the z direction. Structural relaxation of all structures were performed within the framework of DFT, as implemented in the Vienna Ab Initio Simulation Package (VASP).[56] The Perdew, Burke and Ernzerhof functional within the generalized gradient approach was used.[57,58] During the structure optimization, five bottom atomic layers were fixed and ions of rest layers and H3pp molecule were allowed to relax. An energy cutoff of 500 eV and a k-point of $3\times 3 \times 1$ achieve energy and force convergence of 0.01 meV and 20 meV Å^{-1}, respectively. Information on chemical bonding analysis and formation energies of I$^-$ and FA+ vacancies in the reference, H3pp-containing perovskites is presented in Supplemental Information.

Trap density of states (tDOS) measurements by thermal admittance spectroscopy (TAS).[15] Temperature-dependent capacitance measurements were carried out in a temperature-controlled vacuum stage. Capacitance-frequency measurements were carried out in a frequency range of 20 Hz to 2 MHz in logarithmic steps using an Agilent E4980A LCR meter. The capacitance–voltage curve was obtained by measuring the capacitance as the applied d.c. bias voltage was scanned from −0.5 to 1.2 V. Based on the capacitance spectra measured at different temperatures, the trap density (N_T) distribution in energy (E_ω) was calculated with the following relations:

$$N_T(E_\omega) = -\frac{V_{\text{bi}}}{qW}\frac{\mathrm{d}C}{\mathrm{d}\omega}\frac{\omega}{k_{\text{B}}T} \tag{1}$$

$$E_\omega = k_{\text{B}}T \ln\left(\frac{\omega_0}{\omega}\right) = k_{\text{B}}T \ln\left(\frac{2\pi v_0 T^2}{\omega}\right) \tag{2}$$

where V_{bi} is the built-in potential and W is the depletion width (V_{bi} and W are derived from capacitance–voltage measurements); C is the capacitance measured at an angular frequency ω and temperature T; k_{B} is Boltzmann's constant and ω_0 is the attempt-to-escape frequency at temperature T; and v_0 is a temperature-independent constant, which can be obtained by fitting the relation of characteristic frequency with different T based on equation (2).

SUPPLEMENTAL INFORMATION

Supplemental Information can be found online at….

ACKNOWLEDGMENTS

AUTHOR CONTRIBUTION

M.L.-C. conceived the idea.; M.L.-C. and A.H. supervised the study.; M.L.-C. and H.X. prepared the manuscript with support from all coauthors; H.X. and Z.W. designed the experiments, fabricated the devices and measured I-V data.; H.X. carried out different analyses including FTIR, XRD, SEM.; Z.C. and M.P. performed DFT calculations under supervision of S.T.; P.T. and J.A. performed EELS and did the relevant analyses.; D.J.K. and L.E. conducted the solid-state NMR and carried out the relevant analyses.; D.P. assisted with NMR samples preparation.; A.A. performed stability test under operational conditions; X.B. conducted the FIB process for lamellae.; C.P. helped with device fabrication and optimization, and was the responsible for the analysis of thermal stability of devices; H.-S.K. assisted with device fabrication and data analysis. K.G., M.A. and S.S. carried out the TRPL,PLQE and PL analyses.; S.F, X.J., M.B., H.W. and K-J.T carried out the OPTP analyses. X.S and F.F carried out the TAS measurements and CB and FG analysed the TAS data. M.G. and S.M.Z. coordinated the work.

DECLARATION OF INTEREST
The authors declare no competing interests

REFERENCES
1   Kim, H. S. et al. (2012) Lead iodide perovskite sensitized all-solid-state submicron thin film mesoscopic solar cell with efficiency exceeding 9%. Scientific Reports 2, doi:10.1038/srep00591.
2   Lee, M. M., Teuscher, J., Miyasaka, T., Murakami, T. N. & Snaith, H. J. (2012) Efficient Hybrid Solar Cells Based on Meso-Superstructured Organometal Halide Perovskites. Science 338, 643-647, doi:10.1126/science.1228604.
3   Kumar, S., Hodes, G. & Cahen, D. (2020) Defects in halide perovskites: The lattice as a boojum? MRS Bulletin *45*, 478-484, doi:10.1557/mrs.2020.146.

4 Tong, C.-J., Li, L., Liu, L.-M. & Prezhdo, O. V. (2020) Synergy between Ion Migration and Charge Carrier Recombination in Metal-Halide Perovskites. Journal of the American Chemical Society *142*, 3060-3068, doi:10.1021/jacs.9b12391.

5 Fu, L. et al. (2020) Defect passivation strategies in perovskites for an enhanced photovoltaic performance. Energy & Environmental Science *13*, 4017-4056, doi:10.1039/D0EE01767A.

6 Chen, B., Rudd, P. N., Yang, S., Yuan, Y. & Huang, J. (2019) Imperfections and their passivation in halide perovskite solar cells. Chemical Society Reviews *48*, 3842-3867, doi:10.1039/C8CS00853A.

7 Tan, S. et al. (2020) Shallow Iodine Defects Accelerate the Degradation of α-Phase Formamidinium Perovskite. Joule *4*, 2426-2442, doi:https://doi.org/10.1016/j.joule.2020.08.016.

8 Zhang, T., Hu, C. & Yang, S. (2020) Ion Migration: A "Double-Edged Sword" for Halide-Perovskite-Based Electronic Devices. Small Methods *4*, 1900552, doi:10.1002/smtd.201900552.

9 Tan, S. et al. (2020) Steric Impediment of Ion Migration Contributes to Improved Operational Stability of Perovskite Solar Cells. Advanced Materials *32*, 1906995, doi:10.1002/adma.201906995.

10 Lee, J.-W., Kim, S.-G., Yang, J.-M., Yang, Y. & Park, N.-G. (2019) Verification and mitigation of ion migration in perovskite solar cells. APL Materials *7*, 041111, doi:10.1063/1.5085643.

11 Zhang, H., Nazeeruddin, M. K. & Choy, W. C. H. (2019) Perovskite Photovoltaics: The Significant Role of Ligands in Film Formation, Passivation, and Stability. Advanced Materials *31*, 1805702, doi:10.1002/adma.201805702.

12 Ran, C., Xu, J., Gao, W., Huang, C. & Dou, S. (2018) Defects in metal triiodide perovskite materials towards high-performance solar cells: origin, impact, characterization, and engineering. Chemical Society reviews 47 *12*, 4581-4610.

13 Rajagopal, A., Yao, K. & Jen, A. K.-Y. (2018) Toward Perovskite Solar Cell Commercialization: A Perspective and Research Roadmap Based on Interfacial Engineering. Advanced Materials *30*, 1800455, doi:10.1002/adma.201800455.

14 Wang, R. et al. (2019) Constructive molecular configurations for surface-defect passivation of perovskite photovoltaics. Science *366*, 1509-1513, doi:10.1126/science.aay9698.

15 Zheng, X. et al.(2020) Managing grains and interfaces via ligand anchoring enables 22.3%-efficiency inverted perovskite solar cells. Nature Energy *5*, 131-140, doi:10.1038/s41560-019-0538-4.

16 Xie, H. & Lira-Cantú, M. (2020) Multi-component engineering to enable long-term operational stability of perovskite solar cells. J. PhysEnergy *2*, 024008.

17 Pereyra, C., Xie, H. & Lira-Cantu, M. (2020) Additives for Stable Halide Perovskite Solar Cells. J. Energ. Chem. In-Press. doi.org/10.1016/j.jechem.2021.01.037.

18 Braly, I. L. et al. (2018) Hybrid perovskite films approaching the radiative limit with over 90% photoluminescence quantum efficiency. Nature Photonics *12*, 355-361, doi:10.1038/s41566-018-0154-z.

19 Khenkin, M. V. et al. (2020) Consensus statement for stability assessment and reporting for perovskite photovoltaics based on ISOS procedures. Nature Energy *5*, 35-49, doi:10.1038/s41560-019-0529-5.

20 Zhao, Y. et al. (2017) Mobile-Ion-Induced Degradation of Organic Hole-Selective Layers in Perovskite Solar Cells. The Journal of Physical Chemistry C *121*, 14517-14523, doi:10.1021/acs.jpcc.7b04684.

21 Wei, D. et al. (2018) Ion-Migration Inhibition by the Cation–π Interaction in Perovskite Materials for Efficient and Stable Perovskite Solar Cells. Advanced Materials *30*, 1707583, doi:10.1002/adma.201707583.

22 Choi, M.-J. et al. (2020) Functional additives for high-performance inverted planar perovskite solar cells with exceeding 20% efficiency: Selective complexation of organic cations in precursors. Nano Energy *71*, 104639, doi:https://doi.org/10.1016/j.nanoen.2020.104639.

23 Blanchard, J. W., Groy, T. L., Yarger, J. L. & Holland, G. P. (2012) Investigating Hydrogen-Bonded Phosphonic Acids with Proton Ultrafast MAS NMR and DFT Calculations. The Journal of Physical Chemistry C *116*, 18824-18830, doi:10.1021/jp305229s.

24 Li, X. et al. (2015) Improved performance and stability of perovskite solar cells by crystal crosslinking with alkylphosphonic acid ω -ammonium chlorides. Nature Chemistry *7*, 703-711, doi:10.1038/nchem.2324.

25 deQuilettes, D. W. et al. (2016) Photoluminescence Lifetimes Exceeding 8 μs and Quantum Yields Exceeding 30% in Hybrid Perovskite Thin Films by Ligand Passivation. ACS Energy Letters *1*, 438-444, doi:10.1021/acsenergylett.6b00236.

26 Faucon, A. et al. (2013) Fluorescent carboxylic and phosphonic acids: comparative photophysics from solution to organic nanoparticles. Physical Chemistry Chemical Physics *15*, 12748-12756, doi:10.1039/C3CP51369F.

27 Guerrero, G., Alauzun, J. G., Granier, M., Laurencin, D. & Mutin, P. H. (2013) Phosphonate coupling molecules for the control of surface/interface properties and the synthesis of nanomaterials. Dalton Transactions *42*, 12569-12585, doi:10.1039/C3DT51193F.

28 Brown, D. G., Schauer, P. A., Borau-Garcia, J., Fancy, B. R. & Berlinguette, C. P.(2013) Stabilization of Ruthenium Sensitizers to TiO2 Surfaces through Cooperative Anchoring Groups. Journal of the American Chemical Society *135*, 1692-1695, doi:10.1021/ja310965h.

29 Kim, H.-S. et al. (2015) Control of I–V Hysteresis in CH3NH3PbI3 Perovskite Solar Cell. The Journal of Physical Chemistry Letters 6, 4633-4639, doi:10.1021/acs.jpclett.5b02273.

30 Ball, J. M. & Petrozza, A. (2016) Defects in perovskite-halides and their effects in solar cells. Nature Energy *1*, 16149, doi:10.1038/nenergy.2016.149.

31 Yin, W.-J., Shi, T. & Yan, Y. (2014) Unique Properties of Halide Perovskites as Possible Origins of the Superior Solar Cell Performance. Advanced Materials *26*, 4653-4658, doi:10.1002/adma.201306281.

32 Zuo, L. et al. (2017) Polymer-modified halide perovskite films for efficient and stable planar heterojunction solar cells. Science Advances *3*, e1700106, doi:10.1126/sciadv.1700106.

33 Bi, D. et al. (2018) Multifunctional molecular modulators for perovskite solar cells with over 20% efficiency and high operational stability. Nature Communications *9*, 4482, doi:10.1038/s41467-018-06709-w.

34 Wang, L. et al. (2019) A Eu3+/Eu2+ ion redox shuttle imparts operational durability to Pb-I perovskite solar cells. Science *363*, 265-270, doi:10.1126/science.aau5701.

35 Luschtinetz, R., Gemming, S. & Seifert, G. (2011) Anchoring functional molecules on TiO2 surfaces: A comparison between the carboxylic and the phosphonic acid group. The European Physical Journal Plus *126*, 98, doi:10.1140/epjp/i2011-11098-4.

36 Martini, L. A. et al. (2013) Modular Assembly of High-Potential Zinc Porphyrin Photosensitizers Attached to TiO2 with a Series of Anchoring Groups. The Journal of Physical Chemistry C *117*, 14526-14533, doi:10.1021/jp4053456.

37 Zhang, L. & Cole, J. M. (2015) Anchoring Groups for Dye-Sensitized Solar Cells. ACS Applied Materials & Interfaces *7*, 3427-3455, doi:10.1021/am507334m.

38 Bae, E. et al. (2004) Effects of Surface Anchoring Groups (Carboxylate vs Phosphonate) in Ruthenium-Complex-Sensitized TiO2 on Visible Light Reactivity in Aqueous Suspensions. The Journal of Physical Chemistry B *108*, 14093-14101, doi:10.1021/jp047777p.

39 Tress, W. et al. (2018) Interpretation and evolution of open-circuit voltage, recombination, ideality factor and subgap defect states during reversible light-soaking and irreversible degradation of perovskite solar cells. Energy & Environmental Science *11*, 151-165, doi:10.1039/C7EE02415K.

40 Yang, D. et al. (2018) High efficiency planar-type perovskite solar cells with negligible hysteresis using EDTA-complexed SnO2. Nature Communications *9*, 3239, doi:10.1038/s41467-018-05760-x .

41 Jiang, Q. et al. (2019) Surface passivation of perovskite film for efficient solar cells. Nature Photonics *13*, 460-466, doi:10.1038/s41566-019-0398-2.

42 Stranks, S. D. et al. (2013) Electron-hole diffusion lengths exceeding 1 micrometer in an organometal trihalide perovskite absorber. Science *342*, 341-344, doi:10.1126/science.1243982.

43 Stolterfoht, M. et al. (2019) The impact of energy alignment and interfacial recombination on the internal and external open-circuit voltage of perovskite solar cells. Energy & Environmental Science *12*, 2778-2788, doi:10.1039/C9EE02020A.

44 Kim, G. Y. et al. (2018) Large tunable photoeffect on ion conduction in halide perovskites and implications for photodecomposition. Nature Materials *17*, 445-449, doi:10.1038/s41563-018-0038-0.

45 Meggiolaro, D. et al. Iodine chemistry determines the defect tolerance of lead-halide perovskites. Energy & Environmental Science 11, 702-713, doi:10.1039/C8EE00124C (2018).

46 Becker, P. et al. (2019) Low Temperature Synthesis of Stable γ-CsPbI3 Perovskite Layers for Solar Cells Obtained by High Throughput Experimentation. Advanced Energy Materials *9*, 1900555, doi:10.1002/aenm.201900555.

47 Manser, J. S. & Kamat, P. V. (2014) Band filling with free charge carriers in organometal halide perovskites. Nature Photonics *8*, 737-743, doi:10.1038/nphoton.2014.171.

48 Liu, Z. et al. (2020) A holistic approach to interface stabilization for efficient perovskite solar modules with over 2,000-hour operational stability. Nature Energy *5*, 596-604, doi:10.1038/s41560-020-0653-2.

49 Shi, D. et al. (2015) Low trap-state density and long carrier diffusion in organolead trihalide perovskite single crystals. Science *347*, 519-522, doi:10.1126/science.aaa2725.

50 Muscarella, L. A. et al. (2019) Crystal Orientation and Grain Size: Do They Determine Optoelectronic Properties of MAPbI3 Perovskite? The Journal of Physical Chemistry Letters *10*, 6010-6018, doi:10.1021/acs.jpclett.9b02757.

51 Li, N. et al. (2019) Cation and anion immobilization through chemical bonding enhancement with fluorides for stable halide perovskite solar cells. Nature Energy *4*, 408-415, doi:10.1038/s41560-019-0382-6.

52 de Mello, J. C., Wittmann, H. F. & Friend, R. H. (1997) An improved experimental determination of external photoluminescence quantum efficiency. Advanced Materials *9*, 230-232, doi:10.1002/adma.19970090308.

53 Xing, J. et al. (2016) Ultrafast ion migration in hybrid perovskite polycrystalline thin films under light and suppression in single crystals. Physical Chemistry Chemical Physics *18*, 30484-30490, doi:10.1039/C6CP06496E.

54 Zhao, J. et al. (2017) Strained hybrid perovskite thin films and their impact on the intrinsic stability of perovskite solar cells. Science Advances *3*, eaao5616, doi:10.1126/sciadv.aao5616.

55 Yuan, Y. et al. (2015) Photovoltaic Switching Mechanism in Lateral Structure Hybrid Perovskite Solar Cells. Advanced Energy Materials *5*, 1500615, doi:10.1002/aenm.201500615.

56 Kresse, G. & Furthmüller, J. (1996) Efficient iterative schemes for ab initio total-energy calculations using a plane-wave basis set. Physical Review B *54*, 11169-11186, doi:10.1103/PhysRevB.54.11169.

57 Blöchl, P. E. (1994) Projector augmented-wave method. Physical Review B *50*, 17953-17979, doi:10.1103/PhysRevB.50.17953.

58 Perdew, J. P., Burke, K. & Ernzerhof, M. (1996) Generalized Gradient Approximation Made Simple. Phys Rev Lett *77*, 3865-3868, doi:10.1103/PhysRevLett.77.3865.

Figure titles and legends

*Figure 1. PV performance. **a,** SEM cross-sectional image of the PSCs with the H3pp:HP material as the absorber. **b,** Forward and reverse IV curves of the champion H3pp:HP PSC. **c-d,** PCE and V_{oc} statistics of the reference (HP) PSCs (blue) and the H3pp:HP-based PSCs (orange). The boxes show the 25th and 75th percentiles, and the whiskers display the 5th and 95th percentiles. The median and mean are indicated by the dividing lines across the boxes and the open square symbols, respectively. The maximum and minimum values are represented by the cross symbols. **e,** TRPL for the HP (blue) and the 1:500 H3pp:HP ratio (orange) on glass. **f,** OPTP for the HP (blue) and the 1:500 H3pp:HP ratio (orange) on glass.*

Figure 2. Device stability and ion immobilization. a, *Operational stability of PSCs applying RbCsMAFA (●) and CsMAFA (■) with only HP (blue) and with the H3pp:HP (orange), under 1,000 h of continuous illumination at 1 sun under a N_2 atmosphere using white LEDs and MPP tracking. The perovskite is RbCsMAFA, and the H3pp doping ratio is the optimal 1:500. The initial absolute efficiencies are 19.1 % and 19.5 % for the reference and H3pp-PSC (1:500) devices, respectively.* **b,** *OPTP analyses of perovskite films on glass, carried out in N_2 under 4 suns for 10 h.* **c,** *PL measurements carried out on perovskite films on glass in N_2 under 100 suns for 500 sec.* **d,** *Frequency-dependent capacitance of PSCs under 1 sun.* **e,** *Temperature-dependent dark conductivity of HP thin films on glass.*

Figure 3. Effect of H3pp on the perovskite thin film: microstructure and binding mode. *Comparison of the microstructural analysis of the RbCsMAFA (blue) and H3pp:RbCsMAFA 1:500 ratio (orange) thin films:* **a,** *Top-view SEM image.* **b,** *ADF-STEM micrograph (lateral view) of the HP:H3pp 1:500 ratio PSC, and corresponding EELS chemical composition maps of the selected absorber region with a grain boundary (blue rectangle): Individual I (red), P (green) and I + P. The L-edge (132 eV) was applied for the P analysis in the elemental maps.* **c,** *XRD patterns.* **d,** *FTIR analysis of the HP (blue) and HP:H3pp (orange), indicating the peaks corresponding to the P=O stretching mode between 1220 and 1300 nm and the C=O stretching mode between 1600 and 1800 nm.*

Figure 4. Theoretical analysis of the interaction modes between H3pp and FAPbI₃. a, *Example of one dominant interaction mode, where H3pp binds to the FAI-terminated surface of FAPbI₃, forming three hydrogen bonds of two different types.* **b,** *Charge redistribution at the H3pp/FAPbI₃ interface upon the adsorption of H3pp, where charge accumulation and depletion are indicated by yellow and cyan, respectively.* **c,** *Calculated FTIR wavenumbers of the stretching modes of the −C=O and −P=O bonds for H3pp and H3pp-modified FAPbI₃.* **d,** *Formation energy of surface FA and I vacancies in H3pp-modified FAPbI₃ compared with reference FAPbI₃.*

Figure 5. Passivation of shallow point defects in the HP absorber. *Differentiated capacitance spectra (a, d), Arrhenius plots of the inflection frequencies determined from the derivative of the admittance spectra (b, e) and trap density of states (tDOS) deduced from temperature-dependent C–f plots (c, f) for the perovskite solar cells with (d-f) and without H3pp (a-c). The activation energy (E_a) was extracted for each defect and shown inside the figures.*

Supplemental information

Decoupling the effects of defects on efficiency and stability through phosphonates in stable halide perovskite solar cells

Haibing Xie,[1†] Zaiwei Wang,[2†] Zehua Chen,[3] Carlos Pereyra,[1] Mike Pols,[3] Krzysztof Gałkowski,[4] Miguel Anaya,[4] Shuai Fu,[5] Xiaoyu Jia,[5] Pengyi Tang,[1] Dominik Józef Kubicki,[6,7] Anand Agarwalla,[2] Hui-Seon Kim,[2] Daniel Prochowicz,[6,8] Xavier Borrisé,[9] Micha Bonn,[5] Chunxiong Bao,[10] Xiaoxiao Sun,[11] Shaik Mohammed Zakeeruddin,[6] Lyndon Emsley,[7] Jordi Arbiol,[1,12] Feng Gao,[10] , Fan Fu,[11] Hai I. Wang,[5] Klaas-Jan Tielrooij,[1] Samuel D. Stranks,[4] Shuxia Tao,[3] Michael Grätzel,[6] Anders Hagfeldt,[2*] Monica Lira-Cantu[1,2*]

1. Catalan Institute of Nanoscience and Nanotechnology (ICN2), CSIC and the Barcelona Institute of Science and Technology (BIST). Building ICN2, Campus UAB E-08193, Bellaterra, Barcelona, Spain.

2. Laboratory of Photomolecular Science (LSPM), Institute of Chemical Sciences and Engineering, School of Basic Sciences, Ecole Polytechnique Fédérale de Lausanne, CH-1015 Lausanne, Switzerland.

3. Center for Computational Energy Research, Applied Physics, Eindhoven University of Technology, Eindhoven, the Netherlands.

4. Cavendish Laboratory, University of Cambridge, Cambridge, UK.

5. Max-Planck Institute for polymer Research, Ackermannweg 10, Mainz, Germany.

6. Laboratory for Photonics and Interfaces (LPI), Institute of Chemical Sciences and Engineering, School of Basic Sciences, Ecole Polytechnique Fédérale de Lausanne, CH-1015 Lausanne, Switzerland.

7. Laboratory of Magnetic Resonance (LRM), Institute of Chemical Sciences and Engineering, School of Basic Sciences, Ecole Polytechnique Fédérale de Lausanne, CH-1015 Lausanne, Switzerland.

8. Institute of Physical Chemistry, Polish Academy of Sciences, Kasprzaka 44/52, 01-224 Warsaw, Poland.

9. Institute of Microelectronics of Barcelona IMB-CNM, C/del Til·lers., Cjampus Universitat Autònoma de Barcelona (UAB) 08193, Cerdanyola del Vallès (Bellatera), Barcelona, Spain.

10. Department of Physics, Chemistry and Biology (IFM), Linköping University, Linköping, Sweden.

11. Laboratory for Thin Films and Photovoltaics, Empa—Swiss Federal Laboratories for Materials Science and Technology, Ueberlandstrasse 129, Duebendorf, 8600, Switzerland

12. ICREA, Pg. Lluís Companys 23, 08010 Barcelona, Catalonia, Spain.

† These authors contributed equally to this work.

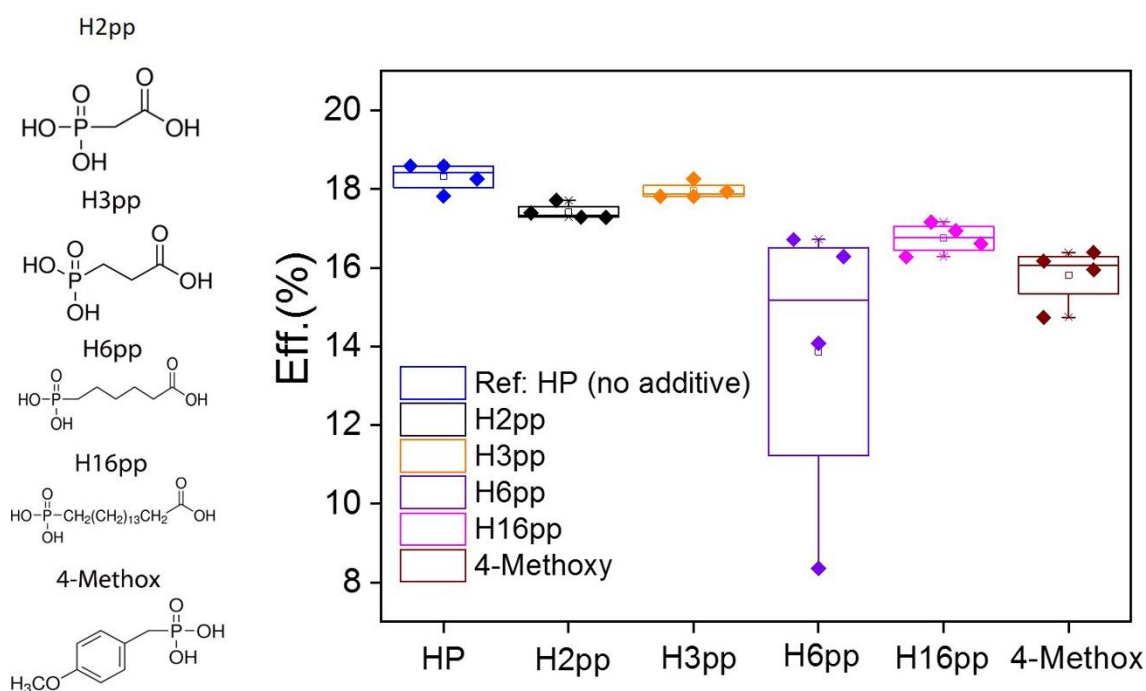* Corresponding authors: anders.hagfeldt@epfl.ch; monica.lira@icn2.cat

Figure S1. Performance of perovskite solar cells doped with different organic additives varying chain length. Additive: perovskite = 1:250 (molar ratio).

To investigate the impact of the functional groups of organic additives on the efficiency and stability of PSCs, we selected molecules with two main functional groups: phosphonic ($-PO(OH)_2$) and carboxylic ($-COOH$) acid groups. These two functional groups were selected due to their optimal interaction with the halide perovskite. The molecules under study varied in chain length and shape: Phosphonoacetic acid (H2PP), 3-Phosphonopropionic acid (H3pp), 6-Phosphonopropionic acid (H6pp) and 16-Phosphonopropionic acid (H16pp). We also tested another organic molecule, 4-Methoxybenzylphosphonic acid (4-Methox), with $-PO(OH)_2$ and methoxide ($-OCH_3$) groups. The effect of these additives on efficiency is summarized in **Figure S1**. We show that among these molecules, H3pp leads to maximum efficiencies, slightly lower than those of the reference devices (18.3 % for the reference versus 18 % with H3pp). Based on the results, we have chosen H3pp as a priority for further investigation and optimization.
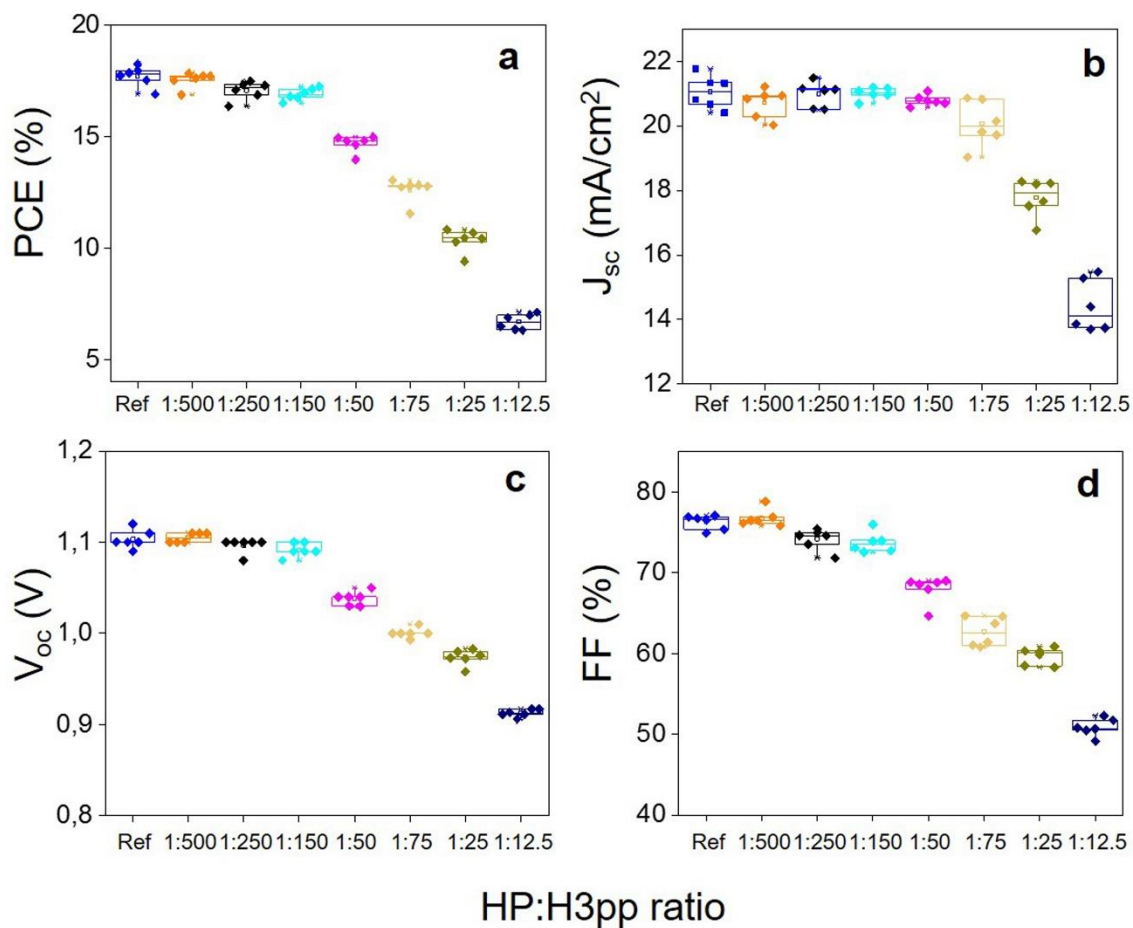
Figure S2. Optoelectronic properties as a function of H3pp doping molar ratio. **a,** power conversion efficiency (PCE), **b,** short circuit current (J_{sc}), **c,** open circuit voltage (V_{oc}) and **d,** fill factor (FF). H3pp: RbCsMAFA perovskite = 1:500, 1:250, 1:150, 1:75, 1:50, 1:25 and 1:12.5 (molar ratio).
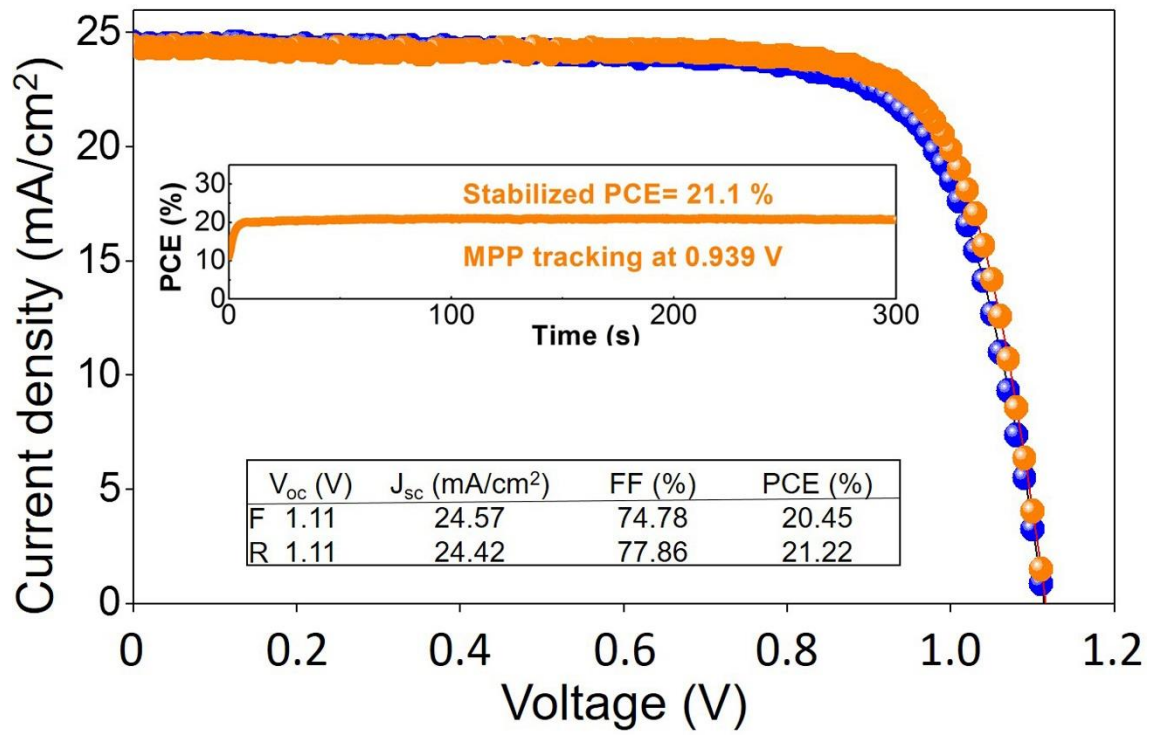
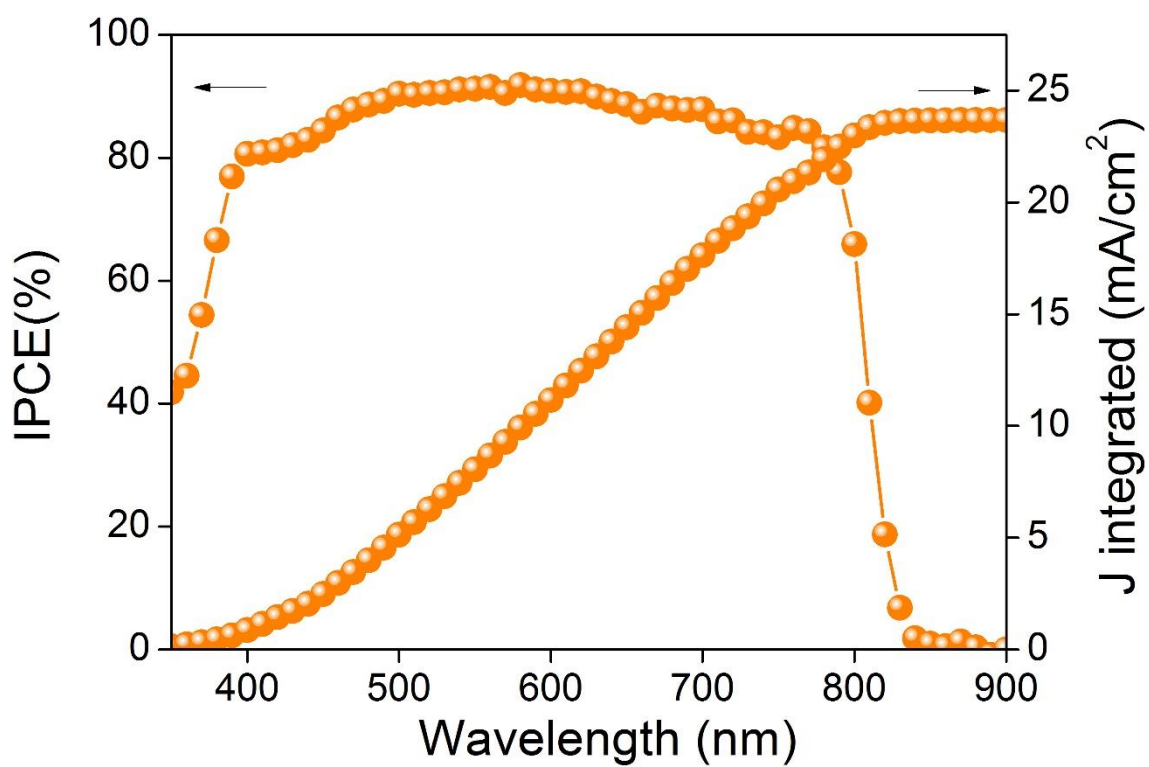**Figure S3.** Optoelectronic parameters of the best device with H3pp: RbCsMAFA perovskite = 1:500 (molar ratio).

Figure S4. IPCE of the champion H3pp-doped RbCsMAFA perovskite solar cell (1:500) shown in Figure 1b and **Supplementary Figure 3**. The integrated J_{sc} for the device is 23.7 mA/cm^2, in agreement with the measured J_{sc} of 24.5 mA/cm^2.
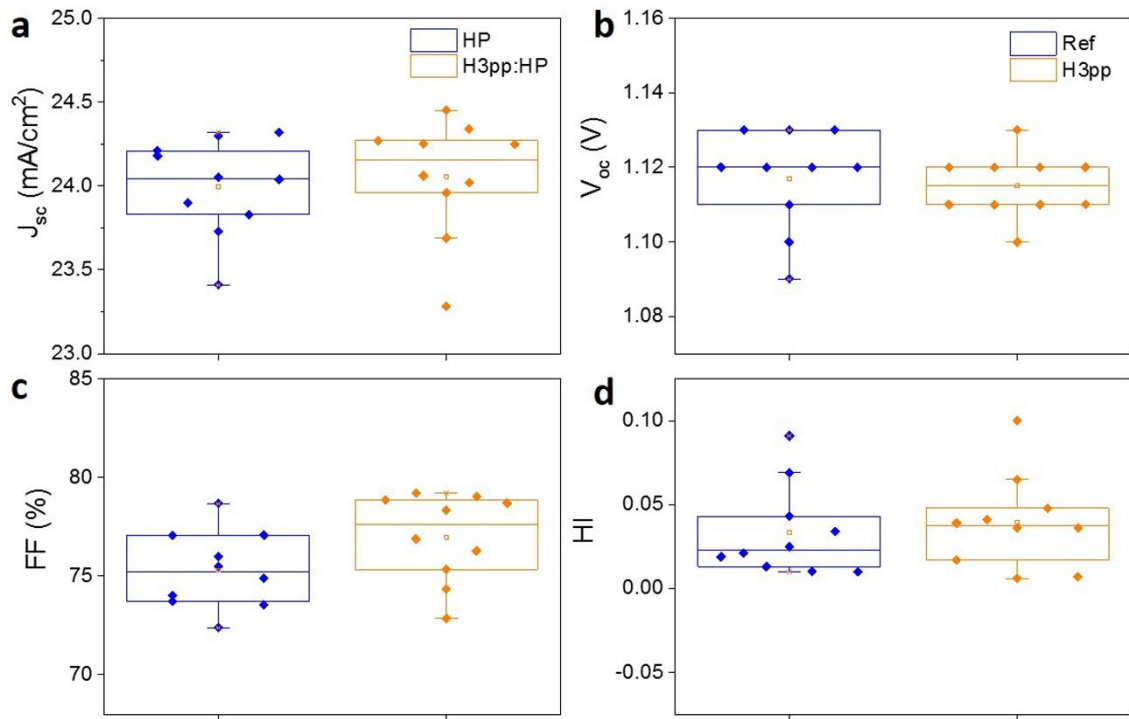
Figure S5. Statistic optoelectronic properties of the reference and H3pp-doped PSCs (1:500): **a,** J_{sc}. **b,** V_{oc}. **c,** FF and **d,** hysteresis index (HI). HI = $(PCE_{Reverse}-PCE_{Foward})/PCE_{Reverse}$.
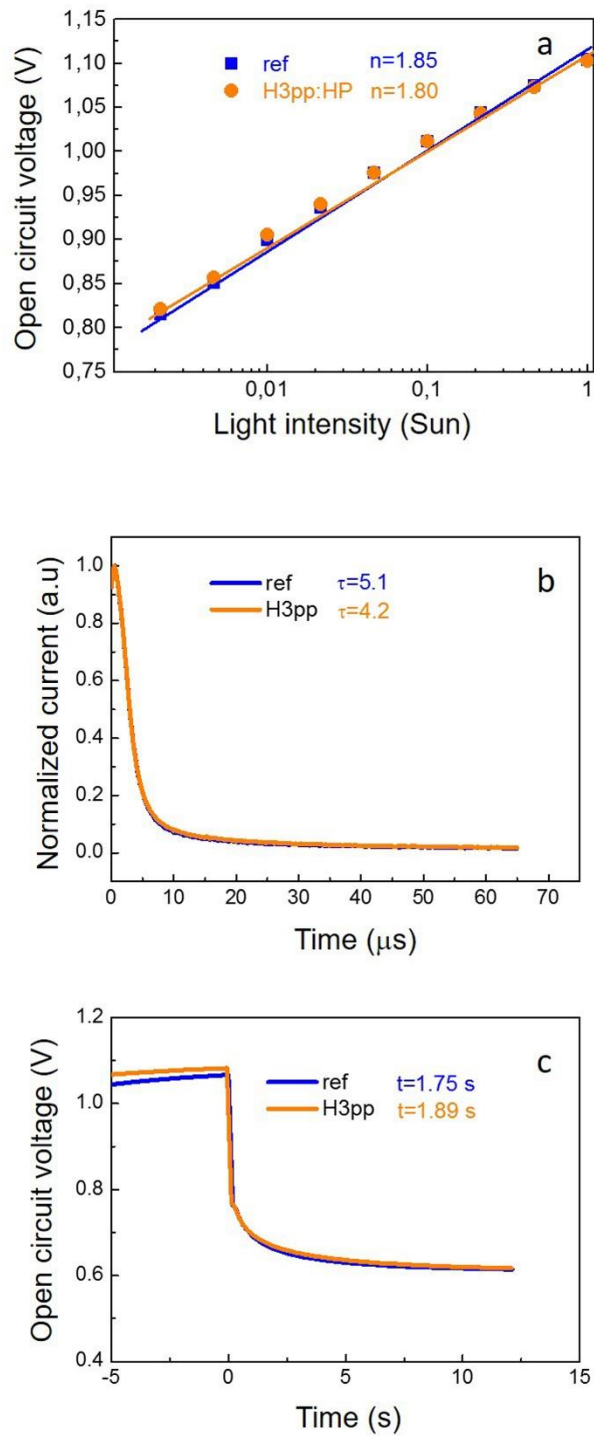
Figure S6. Characterization made to complete PSC devices of the type FTO/c-TiO$_2$/m-TiO$_2$/HP/spiro-OMeTAD/Au with (orange) and without (blue) the H3pp additive. (a) Light intensity dependent V$_{oc}$; (b) Transient photocurrent, and (c) Open circuit voltage decay. In all cases similar Jsc and Voc with (orange) and without H3pp additive (blue) are observed.
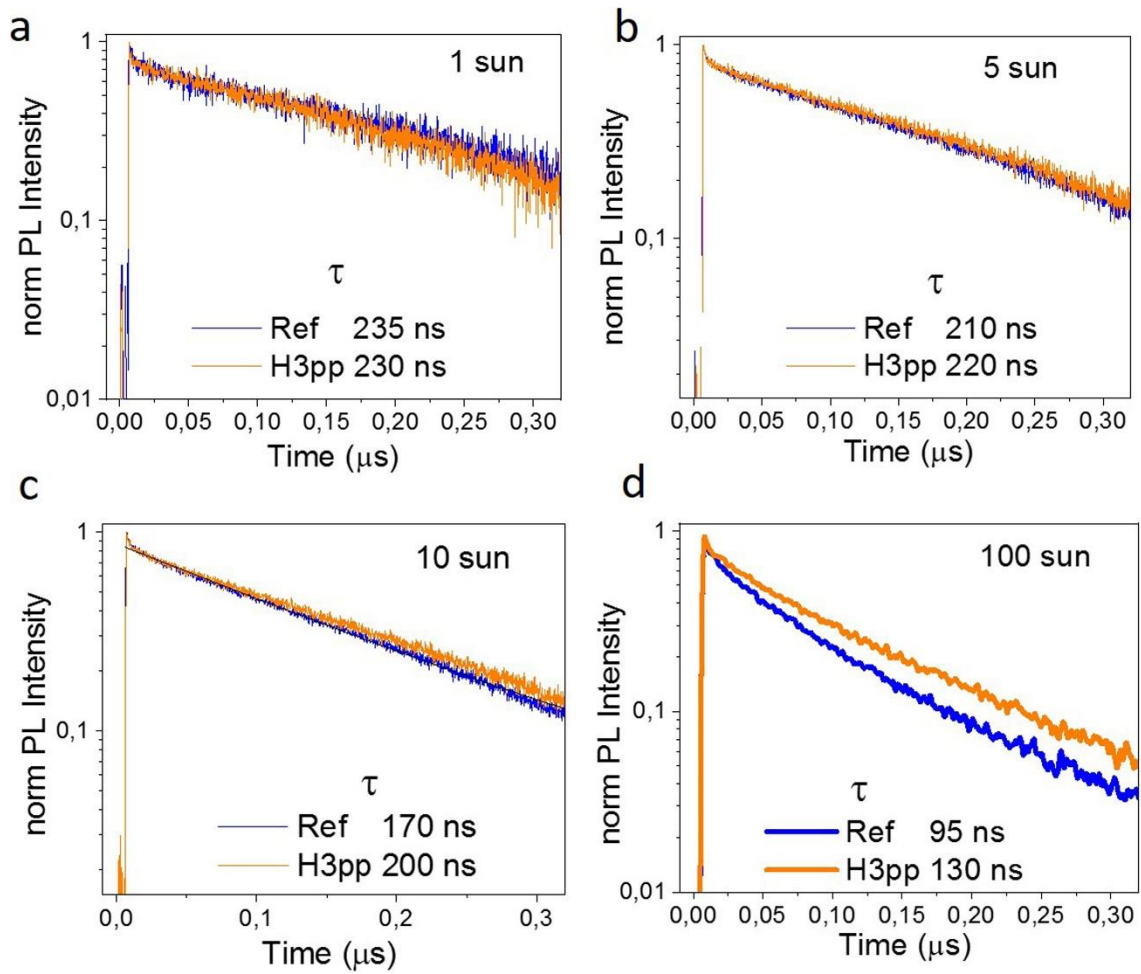
Figure S7. TRPL of the reference and H3pp doped HP under different light intensity (fluences): **a.** 1 sun, **b,** 5 sun, **c,** 10 sun and **d,** 100 sun.
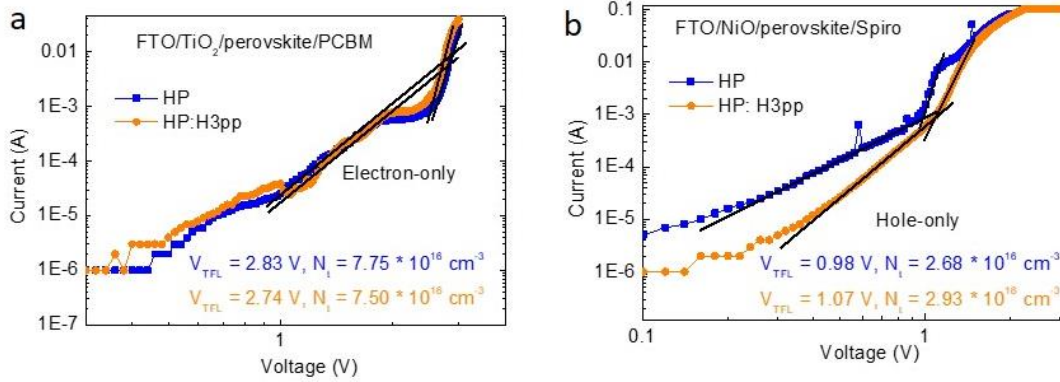
Figure S8. Space-charge-limited current (SCLC) for electron-only (a) and hole-only (b) devices with and without the addition of the H3pp additive.

We carried out SCLC analysis of electron-only devices (**Fig S8a**) and hole-only devices (**Fig S8b**) with and without the H3pp additive. The trap density can be extracted according to the equation: $N_t = 2\varepsilon\varepsilon_0 V_{TFL}/eL^2$, where ε, ε_0, V_{TFL}, e and L represent the relative dielectric constant of perovskite, vacuum permittivity, trap filled limit voltage, elementary charge, and the thickness of the perovskite layer, respectively. Results show that the electron trap density and hole trap density do not change significantly when the H3pp is added. As traps are closely related to deep defects, this result may suggest that the passivation of deep defects is negligible.
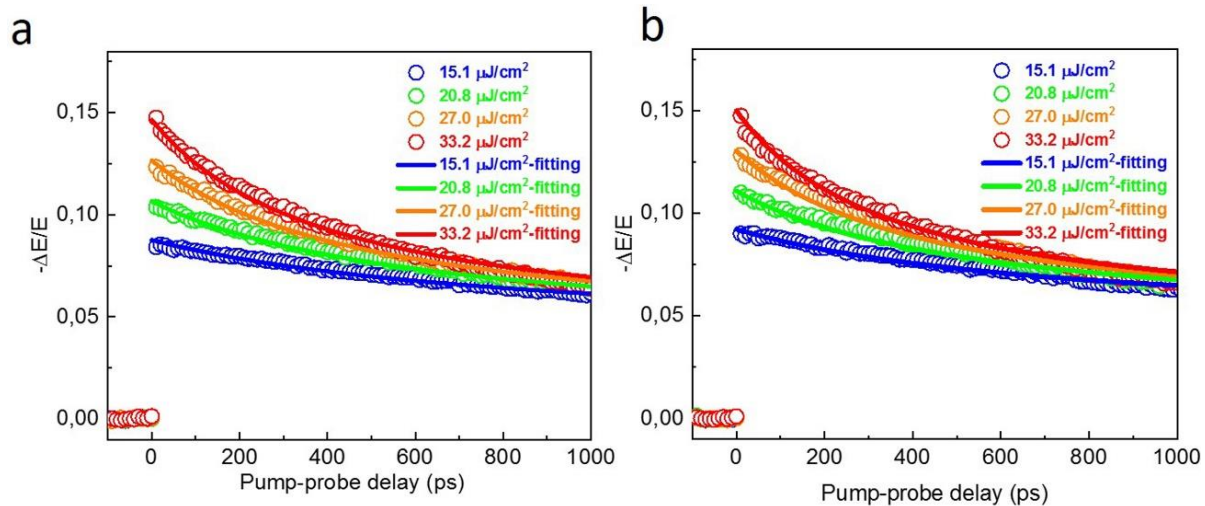
Figure S9. Photoconductivity as a function of pump-probe delay time for reference sample (a) and sample with H3pp additive (1:500) (b), using four different pump fluences (open circles). For both samples, the fluence-dependent dynamics can be described very well by a second order recombination process (only one variable parameter) on top of a flat background (solids lines).
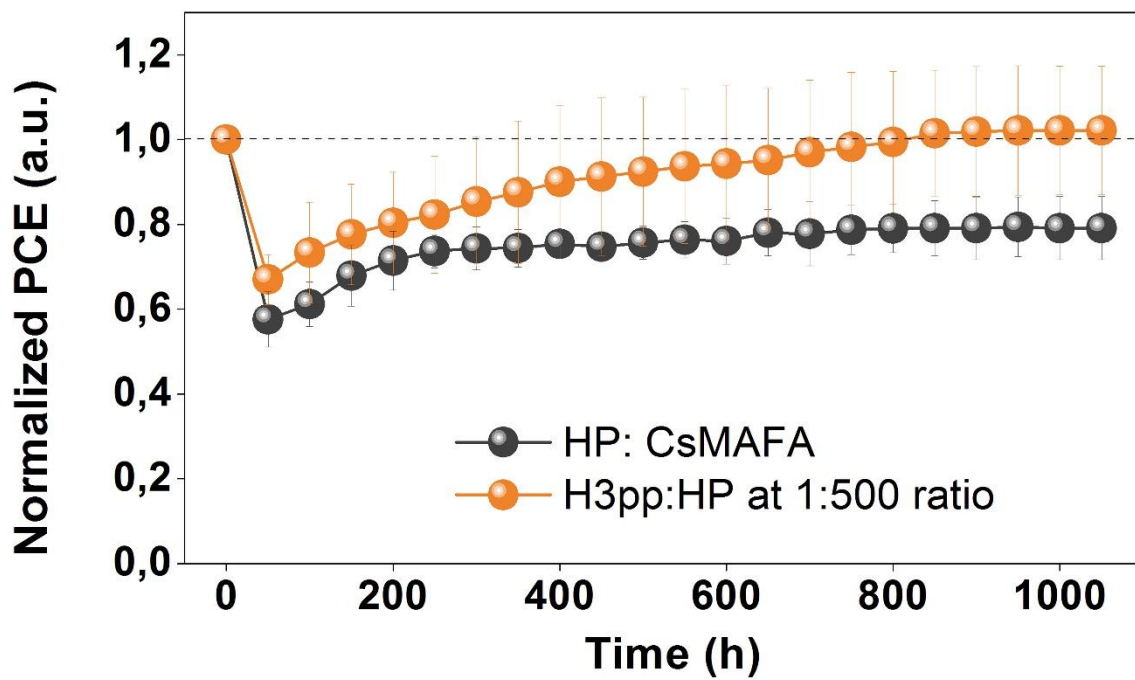
Figure S10. Operational stability of the reference and H3pp-doped (1:500) CsMAFA PSCs under 1,000 h continuous illumination at 1 sun using white LEDs and MPP tracking. 3 devices for each type were employed.
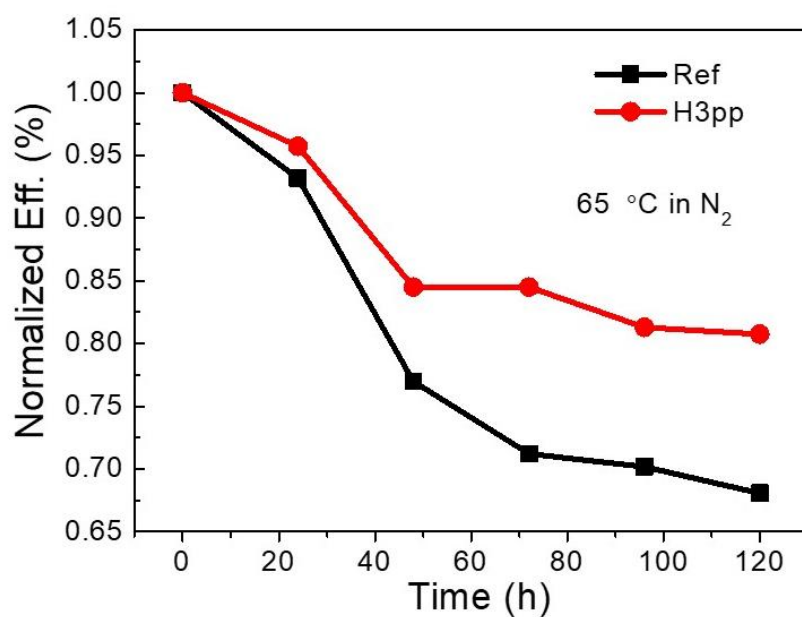
Figure S11. Thermal stability analysis carried out to PSCs under N_2 atmosphere at 65 ºC for 120 h.

The MPP stability was performed at 25 ℃ under N_2 flow without encapsulation (See Experimental section in the main manuscript). To further evaluate the effects of H3pp at a higher temperature, we have carried out thermal stability test of perovskite solar cells with and without addition of H3pp (1:500) in a N_2 glove box at 65 ^{o}C. **Figure S11** shows that after aging at 65 ^{o}C for 120 h in N_2 atmosphere without encapsulation, the device with the addition of H3pp retained over 80% of its original PCE while the reference sample only retained less than 70% of its original PCE. This result demonstrates that H3pp can improve the thermal stability of perovskite solar cells, due to the ability of H3pp on the immobilization of ions.
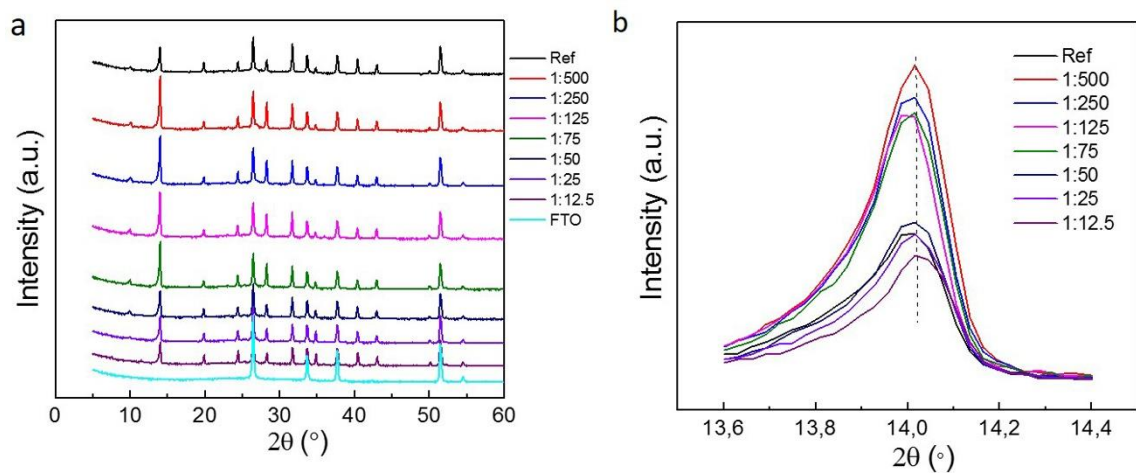
Figure S12. XRD patterns of RbCsMAFA perovskite thin films doped with different concentration of H3pp: **a,** entire patterns with 2θ = 5 - 60°. **b,** enlarged main perovskite peak of (-111), 2θ = 14°.
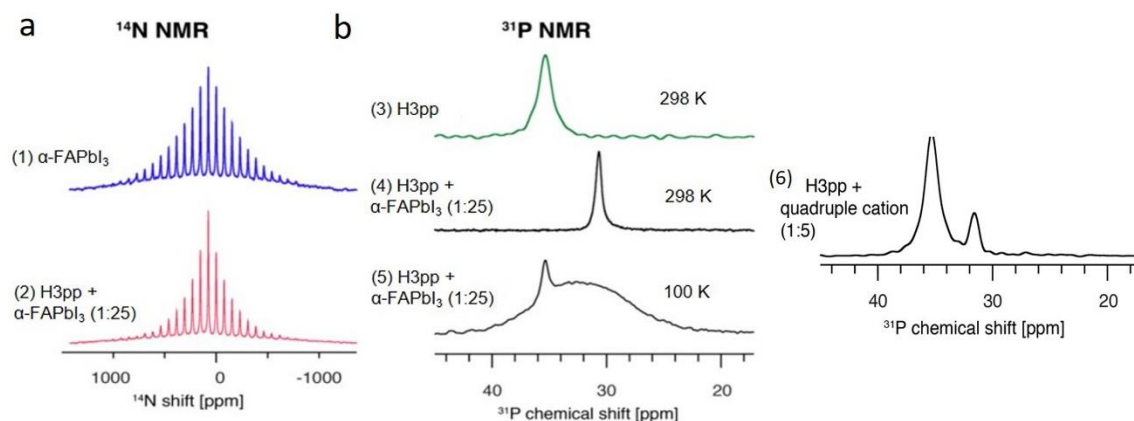
Figure S13. Solid-state nuclear magnetic resonance (NMR). **a,** Nitrogen-14 solid-state magic angle spinning (MAS) NMR spectra (21.1 T, 298 K and 5 kHz) of (1) bulk mechanochemical α-FAPbI$_3$ and (2) H3pp-doped bulk mechanochemical α-FAPbI$_3$ (1:25 mol/mol). **b,** Phosphorus-31 MAS NMR spectra at 21.1 T of (3) neat H3pp (298 K, 12 kHz MAS, echo-detected) and H3pp-doped bulk mechanochemical α-FAPbI$_3$ (1 :25 mol/mol) : (4) at 298 K and 20 kHz MAS (echo-detected) and (5) at 100 K and 12 kHz MAS (^{1}H-^{31}P CP MAS), and (6) H3pp-doped bulk mechanochemical RbCsMAFA perovskite (1:5 mol/mol) at 298 K and 20 kHz MAS (echo-detected).

To verify the interaction of the H3pp with the perovskite crystal lattice we carried out solid-state NMR measurements. To facilitate the interpretation of the NMR results and ensure that they are unambiguous, we first choose the α-FAPbI$_3$ as a simple perovskite model (FA is the dominant cation in the perovskite applied in this work). It should be noted that analogous solid-state NMR analysis can be carried out for the RbCsFAMA perovskite (**Figure S13 b(6)).** However, any small variations in the cation ratio or halide ratio, leading to a very slight change in the cubooctahedral symmetry, would result in a change in the ^{14}N envelope making the interpretation of this result ambiguous. Figure S11a shows the ^{14}N magic angle spinning (MAS) NMR spectra of bulk α-FAPbI$_3$ (**Figure S13 a(1)**) and bulk α-FAPbI$_3$ doped with H3pp (**Figure S13 a(2)),** at 1:25 mol/mol ratio (high doping ratio is required for high quality NMR signal). The ^{14}N spinning sideband (SSB) manifold is narrower in the material doped with H3pp compared to the undoped α-FAPbI$_3$. The width of the ^{14}N SSB manifold is directly related to the symmetry of the cubooctahedral cavity in which FA is reorienting on the picosecond timescale. Narrower SSB manifold corresponds to higher (closer to cubic) symmetry[1,2]. Thus, doping with H3pp results in the modification of the crystallographic symmetry of α-FAPbI$_3$ in such a way that the resulting symmetry is higher. This result indicates that H3pp interacts with the perovskite lattice at the atomic level and has a structure directing effect similar to the previously described for other mono- and bi-functional molecular modifiers[3,4]. We further demonstrate this interaction using ^{31}P MAS NMR (**Figure S13 b**). Pristine H3pp has a ^{31}P chemical shift of 35.4 ppm at 298 K (Figure S11b(3)). In H3pp-doped α-FAPbI$_3$ (1:25 mol/mol) at 298 K (**Figure S13 b(4)**), there is no unreacted H3pp and a new ^{31}P environment is present at 30.7 ppm, corresponding to H3pp interacting with the perovskite lattice. This chemical environment is well defined as indicated by the narrowness of the peak (FWHM: 223 ± 1 Hz). Upon cooling to 100 K, two types of H3pp species are distinguishable in the H3pp-doped perovskite (**Figure S13 b(5)**): a narrow peak at 35.3 ppm (FWHM of about 250 Hz) and a broad peak at 32.6 ppm (FWHM of about 3,000 Hz). The chemical shift of the narrow feature at 100 K matches that

of neat H3pp (note that neat H3pp is not present in this sample, as evidenced by the spectrum at 298 K). In addition, the longitudinal relaxation rate, T_1, of the dipolar coupled protons giving rise to the cross-polarized ^{31}P signal is about 3 s, which is much shorter than the ^{1}H T_1 of the neat H3pp with a value greater than 300 s. The broad peak likely corresponds to H3pp environments that are sensitive to the displacive phase transition of the perovskite lattice (occurring through the octahedral tilt), hence highly disordered at low temperature when the symmetry of the perovskite phase is low. Similar to the model α-FAPbI$_3$ case, there is a new phosphorus environment at 31.6 ppm which corresponds to H3pp interacting with the quadruple cation perovskite lattice on the atomic level (Supplementary **Figure 13 b(6)).** Note that this peak is slightly shifted with respect to that found in the model α-FAPbI$_3$ system (30.7 ppm), due to the presence of the bromide and additional A-site cations in the perovskite lattice, which modifies the local environment sensed by the ^{31}P site of H3pp. Note that the signal of unreacted H3pp is also present in this case, since the doping ratio was higher (1:5). Accordingly, we suggest that the narrow component corresponds to H3pp environments which are farther away from the perovskite surface, thus less sensitive to symmetry lowering. Given this data, it is possible to establish that (i) H3pp modifies the perovskite lattice, likely by binding to its surface (ii) H3pp fully reacts with α-FAPbI$_3$ at 1:25 mol/mol ratio (4 mol %). The possible interaction mode is the formation of a surface layer of H3pp in the GBs and on the surface or the formation of perovskite with H3pp in the hollow cation position[5]. The latter scenario would lead to a significant decrease in the cuboctahedral symmetry (detectable through ^{14}N MAS NMR spectra) as well as leading to new peaks or peak shifts in XRD patterns[6] (Supplementary Figure 10), none of which is observed experimentally. Therefore, we can exclude the hypothesis that H3pp is incorporated into crystal lattice, and conclude that H3pp most likely resides at GBs and on the surface.
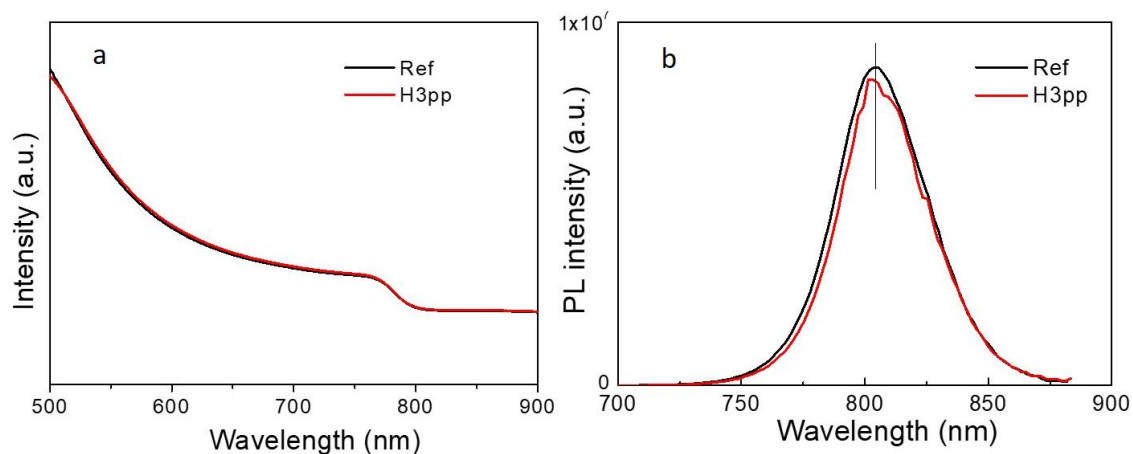
We have performed UV-Vis and PL analyses for the HP and the H3pp:HP samples **(Supplementary Figure 14**). Our results show that there is no obvious difference in the UV-vis and PL spectra when H3pp is added into perovskite precursor, indicating the band gap of perovskite is not influenced. This is consistent with our TRPL and NMR measurement that, H3pp is not incorporated into the perovskite lattice and mainly resides on the surface and in the grain boundaries, passivating mainly shallow defects.
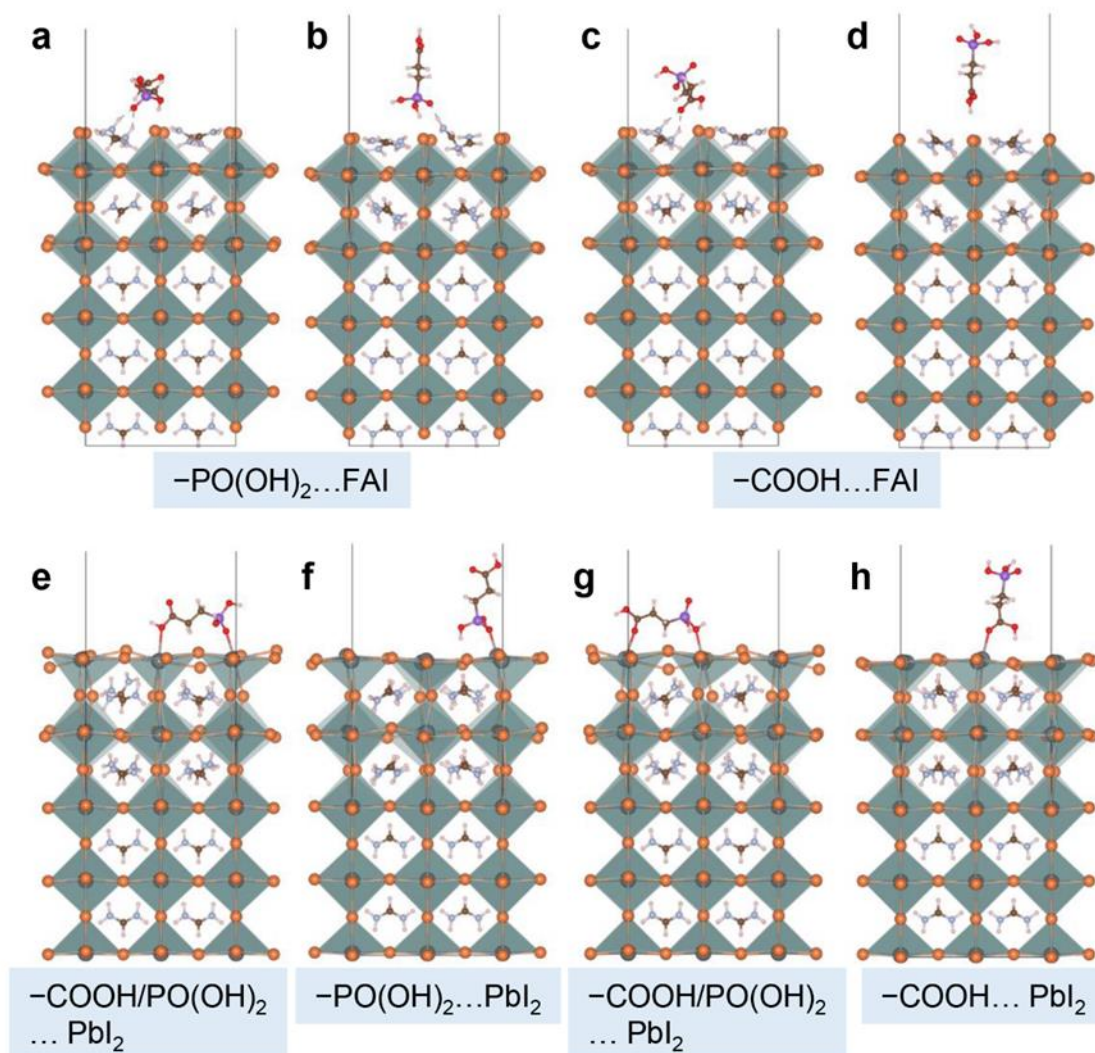
Molecular H3pp: FAPbI₃ interaction modes

Figure S15. H3pp molecule: FAPbI₃ interaction modes on FAI and PbI₂ terminated FAPbI₃ surfaces, ordered by binding energy from the highest to the lowest. **a-b** Functional group −PO(OH)₂ interacts with FAI terminated surfaces, respectively. **c-d** Functional group −COOH interacts with FAI terminated surfaces, respectively. **f** and **h** Functional −PO(OH)₂ and −COOH interact with PbI₂ terminated surfaces, respectively. **e** and **g** Both −COOH and−PO(OH)₂ interact with PbI₂ terminated surface.
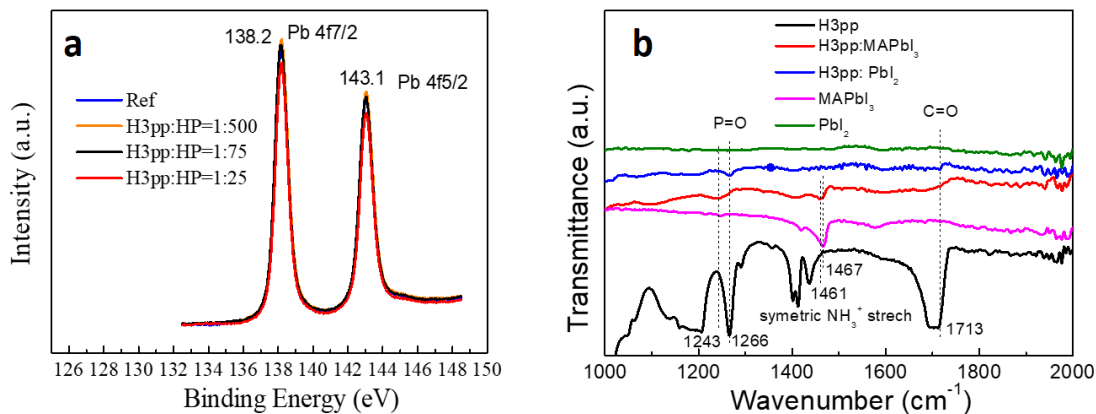
Figure S16. (a) XPS analysis of the HP and the H3pp:HP with different concentration of the additive H3pp. (b) FTIR analyses of the MAPbI₃ (MAPI), the H3pp, the PbI₂ and the combination of H3pp with MAPI and PbI₂.

XPS analyses carried out to the fresh perovskite with and without the H3pp varying the H3pp: HP ratio are shown in the **Figure S16a**. We can observe no shift of the Pb peaks, indicating negligible interaction of the H3pp molecule with Pb. In addition, we have also included FTIR spectra carried out on several samples with and without the H3pp (**Figure S16b**), which shows that the -P=O peak of the H3pp does not shift in a mixture of H3pp:PbI₂, while it shifts to a lower position when the halide perovskite is added (H3pp:MAPbI₃). Therefore, both XPS and FTIR experimental results as well as our DFT calculations (Fig.4) confirm that, H3pp interacts with the perovskite mainly through hydrogen bonding of the organic cations and iodine, and not through the coordination with Pb. This supports our model that H3pp mainly passivate the shallow defects (e.g., V_{MA}, V_{FA}, V_I vacancies) and not passivate the deep defects (e.g., Pb_I antisite defects).
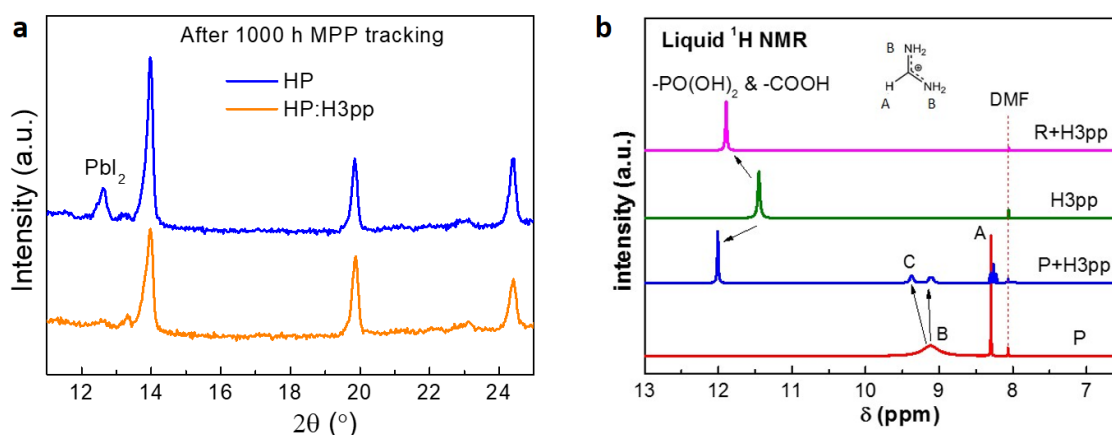
Figure S17. (a) XRD analyses of the perovskite samples with and without the H3pp additive, after 1000 h under continuous light irradiation of 1 sun, MPP tracking, N_2 atmosphere, RT. (b) Liquid-state ^1H NMR spectra of the neat H3pp, the RbPbI₃:H3pp (R+H3pp), perovskite:H3pp (P+H3pp) mixtures and the neat perovskite (P). Here perovskite is RbCsMAFA. To ensure the detection resolution, RbCsMAFA (or RbPbI₃): H3pp= 2.5:1 was prepared in 0.5 mL DMF-d7.

Figure S17a shows the XRD spectra of perovskite solar cells after 1000 h MPP tracking under one sun continuous irradiation. The devices with H3pp addition show negligible PbI_2 while the control devices show a prominent PbI_2 peak, demonstrating that the H3pp effectively prevents perovskite decomposition. To further confirm the interaction of H3pp with perovskite (RbCsMAFA), we have performed liquid-state ^1H NMR spectra of the neat H3pp, the RbPbI₃:H3pp (R+H3pp, 2.5:1), perovskite:H3pp (P+H3pp, 2.5:1) mixtures and the neat perovskite (P), as shown in **Figure S17b**. The ^1H NMR spectrum of the neat H3pp in solution shows a peak located at δ = 11.4 ppm, which corresponds to the $-PO(OH)_2$/$-COOH$ groups. Note that it is undistinguishable for the $-PO(OH)_2$ and $-COOH$ group due to a very similar chemical shift. The presence of RbPbI₃ or the perovskite in the H3pp (R+H3pp and P+H3pp), induces a downfield chemical shift of 0.4 ppm and 0.6 ppm for the $-PO(OH)_2$/$-COOH$, respectively. This is attributed to the formation of hydrogen bonds between the halides (I^- and Br^-) and the acidic protons of $-PO(OH)_2$/ $-COOH$, consistent with stronger proton deshielding in O-H···I^- (Br^-) compared to O-H. The ^1H NMR spectrum of perovskite in solution reveals a peak at δ = 8.3 ppm (labelled "A"), ascribed to the C-H protons of the FA moiety, while the broad peak at δ = 9.1 ppm (labelled "B") belongs to the $-NH_2$ protons in FA (inset). After the addition of H3pp into the perovskite solution (P+H3pp), a new peak (labelled "C") at δ = 9.4 ppm appears next to peak B. This peak is assigned to $-NH_2$ protons in a new chemical environment and leads to more splitting of the neighbouring peak A. This data suggests that FA forms hydrogen bonds with H3pp through the $-NH_2$ group, most likely of the following form: -P=O···H or -C=O···H, since the deshielding effect of the π electrons leads to a downfield shift of the $-NH_2$ signals in the P+H3pp mixture. In summary, liquid-state ^1H spectra show that H3pp interacts with both organic cations and halide anions in perovskite via hydrogen bonding, which is consistent with the FTIR and DFT calculations in the manuscript.
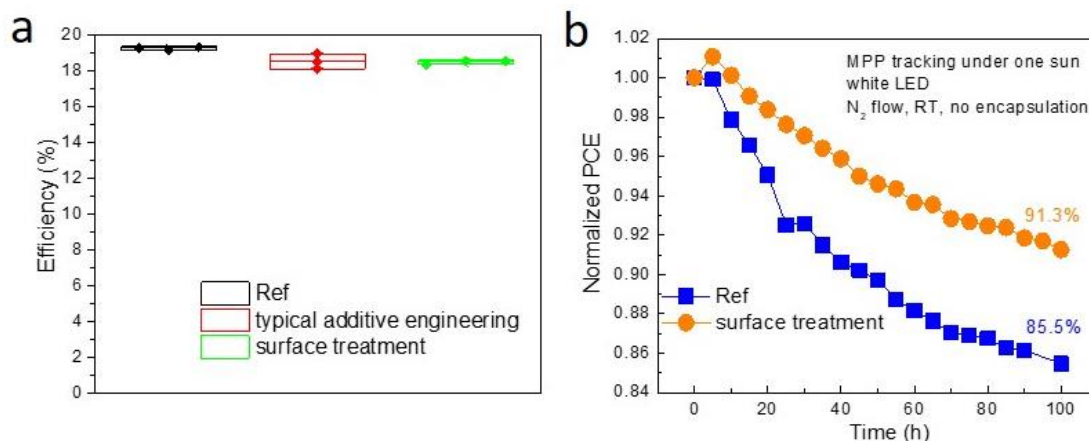
Figure S18. Comparison of different passivation methods. (a) Power conversion efficiency of PSCs without the H3pp additive (black), typical additive engineering with the H3pp additive added to the perovskite precursor solution (red) and surface treatment with the H3pp dissolved in isopropanol (IPA) and added on top of the perovskite thin film (green). (b) MPP tracking of devices without (Ref) and with the surface treatment of H3pp for 100 h.

We have carried out analysis of the performance of the reference PSCs device (without H3pp), the device made by the typical additive engineering method (adding the H3pp in the perovskite precursor as in the manuscript), and the device made by surface treatment of the halide perovskite film (dissolving the H3pp in isopropanol and adding it to the surface of the halide perovskite by spin coating. It should be noted that H3pp is insoluble in solvents like chlorobenzene required for the preparation of PSC by the antisolvent method). Results, shown in **Figure S18a**, indicate that the surface treatment of the halide perovskite with the H3pp (**Figure S18a**, green) results in devices of comparable efficiencies with those of the reference device (**Figure S18a,** black) and those fabricated by the typical additive engineering method reported in this work (**Figure S18a,** red). Additionally, surface treatment of the perovskite film with the H3pp additive can also improve the operational stability of perovskite solar cells if compared to the reference PSC without the H3pp additive (**Figure S18b**). Although the stability is not as good as the one obtained by adding the H3pp into the perovskite precursor solution (as in this manuscript), the results demonstrate that the surface treatment with H3pp improves PSC stability.
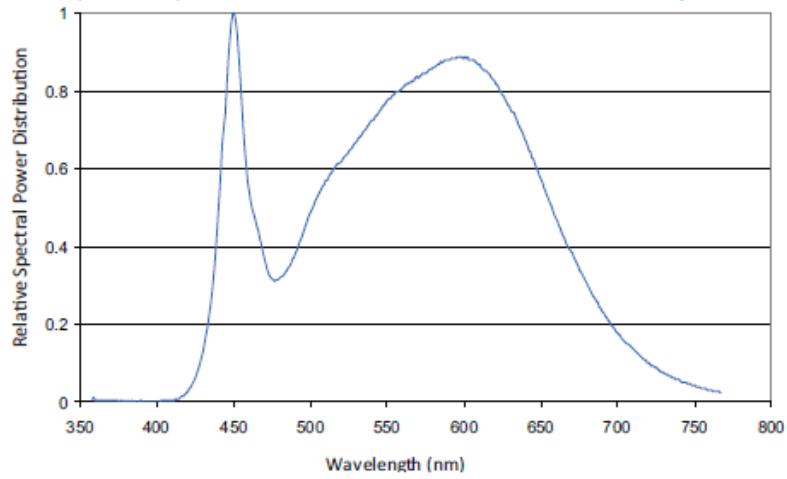
Figure S19. Emission spectrum of the white LEDs used in the stability test.

Table S1. Measured PLQE and estimated QFLS of HP thin films and devices with and without H3pp under one sun.

Configuration	HP		H3pp:HP 1:500	
	PLQE	QFLS (eV)	PLQE	QFLS (eV)
a. Glass/Perovskite HP	1.90 %	1.232	1.94 %	1.232
b. Glass/c-TiO$_2$/m-TiO$_2$/Perovskite HP/Spiro-OMeTAD	0.007 %	1.087	0.004 %	1.074

Quasi-Fermi level splitting (QFLS) determines the theoretical limit of V_{oc} can be obtained for HP and PSCs ($V_{oc,limit}$ = QFLS/q, where q is the elemental charge). The equation to calculate the QFLS from PLQE is[7]:

$$QFLS = kT \ln(PLQE * J_G / J_{0,rad})$$

Where k is the boltzmann constant, T is the temperature, $J_{0,rad}$ is the radiative thermal equilibrium recombination current density in the dark, J_G is the generated current density under illumination. For estimation, we assume J_G = J_{sc} = 220 A*m^{-2}, $J_{0,rad}$ = 6.5*10^{-21} A*m^{-2} (typical value from the literature), the QFLS values are estimated to be 1.232 eV for the ref and H3pp doped HP, and 1.087eV and 1.074 eV for the ref and H3pp doped PSCs, respectively. Indeed, the same batch of devices of Ref and 1:500 have an average V_{oc} of 1.07 V and 1.06 V, respectively. In sum, the PLQE results confirm the similar non-radiative recombination in the HP thin films and devices with and without H3pp.

Table S2. Binding energy, vibrational frequency of relevant bonds in H3pp molecule: FAPbI$_3$ systems in **Supplementary Figure 12.**

Configurations		Binding energy (eV)	Frequency (cm^{-1})	
			−C=O	−P=O
FAI termination	**a**	**3.13**	**1756.58**	**1171.42**
	b	**2.99**	**1752.63**	**1207.14**
	c	2.93	1693.86	1244.14
	d	2.90	1733.14	1244.52
PbI$_2$ termination	e	2.54	1764.79	1182.36
	f	1.91	1753.00	1097.63
	g	1.84	1692.72	1276.74
	h	1.59	1642.62	1234.21

Note I: Spin-polarized DFT framework for charged defect formation energy calculations.

We calculated the formation energies of FA$^+$ and I$^-$ at the FAI terminated surface of the H3pp - modified FAPbI$_3$, respectively. As a reference, we also calculate the same formation energies for the pristine FAI terminated FAPbI$_3$. The defect formation energy is given as,

$$DEF(X^q) = E(X^q) - E(bulk) - \sum_i n_i \mu_i + q(E_F + E_{VBM} + \Delta V)$$

(0.1)

where $E(X^q)$ is the total energy of the defect system with charge q, $E(bulk)$ is the total energy of the pristine system, and n and μ are the number and the chemical potentials of the species added to or subtracted from the perfect system in order to form the defect. The last term is the energy associated with the exchange of charges with the electrons' reservoir (the Fermi level of the system E_F), referenced to the valence band maximum (E_{VBM}) of the pristine system, followed by a correction for the electrostatic potential shift ΔV induced by the defect.

The last term is assumed to be the same for H3pp-modofied and -unmodified FAPbI$_3$ because similar Quasi Fermi level splitting (QFLS) for the two perovskites is found in photoluminescence quantum efficiency (PLQE) observations (**Supplementary Table 1**). We define the relative formation energy as in Ref. 8. The suppression of FA$^+$ and I$^-$ vacancy formation due to the introduction of H3pp molecule is quantitatively evaluated by,

$$\Delta\Delta E_{vac} = DEF(X^q, H3pp) - DEF(X^q, ref)$$

(0.2)

where $DEF(X^q, H3pp)$ is the formation energy of a FA or I vacancy in the presence of H3pp molecule and $DEF(X^q, ref)$ the one of the unmodified FAI-terminated surface.

References

1. Kubicki, D. J. et al. (2017) Cation dynamics in mixed-cation (MA)x(FA)1–xPbI3 hybrid perovskites from solid-state NMR. J. Am. Chem. Soc. *139*, 10055-10061.
2. Kubicki, D. J. et al. (2018) Formation of stable mixed guanidinium–methylammonium phases with exceptionally long carrier lifetimes for high-efficiency lead iodide-based perovskite photovoltaics. J. Am. Chem. Soc. *140*, 3345-3351.
3. Bi, D. et al. (2018) Multifunctional molecular modulators for perovskite solar cells with over 20% efficiency and high operational stability. Nat. Commun. *9*, 4482.
4. Tavakoli, M. M. et al. (2018) Addition of adamantylammonium iodide to hole transport layers enables highly efficient and electroluminescent perovskite solar cells. Energy Environ. Sci. *11*, 3310-3320.
5. Spanopoulos, I. et al. (2018) Unraveling the chemical nature of the 3D "hollow" hybrid halide perovskites. J. Am. Chem. Soc. *140*, 5728-5742.
6. Mei, A. et al. (2014) A hole-conductor–free, fully printable mesoscopic perovskite solar cell with high stability. Science *345*, 295-298.
7. Stolterfoht, M. et al. (2019) The impact of energy alignment and interfacial recombination on the internal and external open-circuit voltage of perovskite solar cells. Energy Environ. Sci. *12*, 2778-2788, doi:10.1039/C9EE02020A.
8. Li, N., Tao, S., Chen, Y. et al. (2019) Cation and anion immobilization through chemical bonding enhancement with fluorides for stable halide perovskite solar cells. Nat. Energy *4*, 408–415. https://doi.org/10.1038/s41560-019-0382-6.